Continental Shelf Research 76 (2014) 36–52

Contents lists available at ScienceDirect

Continental Shelf Research

journal homepage: www.elsevier.com/locate/csr

Research papers

Wastewater effluent dispersal in Southern California Bays

Yusuke Uchiyama [a,*], Eileen Y. Idica [b], James C. McWilliams [c], Keith D. Stolzenbach [d]

[a] Department of Civil Engineering, Kobe University, Kobe, Japan
[b] Trussell Technologies, Inc., San Diego, CA 92075, USA
[c] Department of Atmospheric and Oceanic Sciences, University of California, Los Angeles, CA 90095-1565, USA
[d] Department of Civil and Environmental Engineering, University of California, Los Angeles, CA 90095-1593, USA

ARTICLE INFO

Article history:
Received 18 March 2013
Received in revised form
1 October 2013
Accepted 2 January 2014
Available online 18 January 2014

Keywords:
Regional ocean modeling
Sewage dispersal
Submesoscale stirring
Urban wastewater

ABSTRACT

The dispersal and dilution of urban wastewater effluents from offshore, subsurface outfalls is simulated with a comprehensive circulation model with downscaling in nested grid configurations for San Pedro and Santa Monica Bays in Southern California during Fall of 2006. The circulation is comprised of mean persistent currents, mesoscale and submesoscale eddies, and tides. Effluent volume inflow rates at Huntington Beach and Hyperion are specified, and both their present outfall locations and alternative nearshore diversion sites are assessed. The effluent tracer concentration fields are highly intermittent mainly due to eddy currents, and their probability distribution functions have long tails of high concentration. The dilution rate is controlled by submesoscale stirring and straining in tracer filaments. The dominant dispersal pattern is alongshore in both directions, approximately along isobaths, over distances of more than 10 km before dilution takes over. The current outfall locations mostly keep the effluent below the surface and away from the shore, as intended, but the nearshore diversions do not.

1. Introduction

Coastal oceans are discharge sites for agricultural, industrial, and urban pollution around the world; they are also places with dense human and wildlife populations and fisheries. Pollution management of offshore effluent is necessary and relies on treatment in reducing toxicity, and dispersal and dilution by ocean currents to reduce local concentration levels.

Urban treated wastewater (sewage) from greater Los Angeles has three major effluent discharge pipes, two of which are considered here. One is near Huntington Beach in San Pedro Bay (SPB, extending south from Palos Verdes Peninsula past Newport Beach) and is run by the Orange County Sanitation District (OCSD), while the other is near the Hyperion Treatment Plant (HTP) in Santa Monica Bay (SMB, extending between Point Dume and Palos Verdes Peninsula) and is run by the City of Los Angeles Bureau of Sanitation. Both have offshore outfalls below the surface within embayments and inshore of the strongest currents.

In this paper we simulate effluent dispersal and dilution using a circulation model that has multiply nested grids from a regional configuration for the U.S. West Coast with mesoscale horizontal grid resolution ($dx=5$ km) down to the SPB and SMB subdomains with submesoscale grid resolution ($dx=75$ m). The nesting approach is necessary to represent the influence of larger scale currents on the local ones by which the dispersal occurs. We choose the particular period of Fall 2006 to obtain a representative range of dispersal behaviors. Model forcing is by synoptic meteorological surface fields (themselves were generated in a nested meteorological model) and by lateral open boundary conditions constructed from the output of a global oceanic model with data assimilation and from an empirical tidal analysis. This configuration is intended as comprehensive for all relevant types of currents within this class of model formulation.

A regional coastal model with a nested-grid hierarchy can serve many purposes. We use the Regional Oceanic Modeling System (ROMS) whose principal algorithms are described in Shchepetkin and McWilliams (2005, 2008) and nesting techniques in Penven et al. (2006) and Mason et al. (2010). Using ROMS configurations similar to the one used here (Section 2.1), the simulation and empirical validation of the regional circulation and eddy characteristics are made for the U.S. West Coast in Marchesiello et al. (2003) and Capet et al. (2008a) and for the Southern California Bight (containing SPB and SMB) in Dong et al. (2009). Particular process studies are made for island wakes (Dong and McWilliams, 2007); upwelling events (Capet et al., 2004; Dong et al., 2011); mesoscale eddy distribution (Kurian et al., 2011) and buoyancy flux (Colas et al., 2013); California Undercurrent separation and its submesoscale instability (Molemaker et al., 2014); tidal currents (Wang et al., 2009; Buijsmann et al., 2012); sediment transport (Blaas et al., 2007); nearshore particle dispersion (Romero et al., 2013); plankton productivity (Gruber et al., 2006, 2012); and larval dispersal and connectivity (Carr et al., 2008; Mitarai et al., 2009).

* Corresponding author.
E-mail addresses: uchiyama@harbor.kobe-u.ac.jp (Y. Uchiyama), eileen.idica@trusselltech.com (E.Y. Idica), jcm@atmos.ucla.edu (J.C. McWilliams), stolzenb@ucla.edu (K.D. Stolzenbach).

0278-4343/$ - see front matter © 2014 Elsevier Ltd. All rights reserved.
http://dx.doi.org/10.1016/j.csr.2014.01.002

Besides including the effluent sources (Section 2.2), the present circulation and associated dispersal study is novel by incorporating smaller scale features and analyzing them closer to shore.[1] Compared to the persistent currents and mesoscale eddies that dominate the flow in deeper water offshore, the important local agents of wastewater effluent transport are the currents over the continental slope and shoaling shelf. They are comprised of mesoscale and submesoscale eddies (including poleward-propagating coastally trapped waves), and both barotropic and internal tides (Hickey, 1992; Kim et al., 2010). Some coastal waves are generated by wind fluctuations that are located equatorward of the model domain and have a smaller scale than is resolved in the open boundary condition fields; these are absent in our simulations, although regionally generated coastal waves are present. Submesoscale currents arise from frontogenesis and baroclinic instability processes in the surface layer (Capet et al., 2008b) and topographic and coastline shear wakes (Dong et al., 2009; Molemaker et al., 2014). Our configuration lacks surface gravity wave effects, so littoral currents in the surf zone are absent, hence this final step of effluent transport to the shoreline is missing. (We hope to address this later.) The focus here is not as much on these different types of currents and their dynamical processes but rather on the resulting effluent distributions they cause.

In Southern California discharge of wastewater effluent into the ocean was historically implemented as a way to safely dispose of minimally treated (*e.g.*, screening only) sewage with the understanding that dilution within the ocean would render the harmful constituents safe via biological and chemical reactions and physical transport. However, environmental concerns grew, and the municipalities began implementing increased treatment (*e.g.*, primary sedimentation, secondary biological treatment) on land as well as placing outfalls further offshore and at greater depth (SCCWRP, 1973; Anderson et al., 1993; Sklar, 2008). Outfall design also often included diffusers consisting of a pipe with discharge jets under pressure through multiple ports over a length approximately 10 times the discharge depth. This design enabled greater immediate mixing through the individual jets, followed by increased nearfield mixing and dilution of the turbulent buoyant plume, as compared to a single pipe outlet (Fischer et al., 1979). Both OCSD and HTP have primary outfalls that follow this design rationale, with outfalls that terminate approximately 5 miles offshore with multi-port, bottom-mounted diffusers at depths of $h=60$ m and 57 m, respectively (CRWQCB, 2010, 2012). Each currently discharged secondary-treated wastewater effluent, which typically has elevated levels of nitrogen (as ammonia and/or nitrate), organic matter, and pathogens relative to the receiving ocean waters. Both effluent and receiving waters are monitored for these conventional pollutants and for numerous other contaminants (inorganic, volatile and non-volatile organics, carcinogens, *etc.*) that might affect human and environmental health.

The effluent plumes of both the OCSD and HTP outfalls have been found to remain primarily subsurface below depths of 15–20 m during typical density-stratified conditions, as detected by a variety of parameters (salinity, colored dissolved organic matter, bacteria, ammonia) during routine monitoring (OCSD, 2012; City of Los Angeles, 2007). The routine monitoring stations used by the agencies extend about 10 km perpendicular from shore, and thus are not ideal for tracking the horizontal extents of the plumes. Jones et al. (2001) detected the OCSD effluent plume at least 12.5 km from the outfall in either alongshore direction during two sampling periods using salinity, ammonium, and fecal coliform bacteria as indicators. Boehm et al. (2002) investigated cross-shelf transport of the OCSD effluent plume towards the shore and found the plume within approximately 2 km of the shore (5 km from the outfall), as indicated by *E. coli*. Jones (2004) found consistent results in plume sampling for cross-shelf transport using salinity, fecal indicator bacteria, and ammonium as evidence of plume presence. In general, studies of the OCSD effluent plume have shown mainly alongshore transport either up or downcoast from the outfall, over subsurface depths ranging from 15 to 70 m, and with considerable heterogeneity in plume patterns (Jones et al., 2001; Boehm et al., 2002; Jones, 2004; Todd et al., 2009). Effluent plume surfacing appears rare, although evidence of the HTP effluent plume on the surface has been captured by synthetic aperture radar (SAR) imagery during one winter event in 1997, with the plume covering an area of approximately 16 km^2 above the diffuser location (Di Giacomo et al., 2004).

The current OCSD and HTP outfalls have been in continuous operation for 40–50 years. To perform any major repairs or internal inspection of the structures, the effluent needs to be diverted to another location. For both facilities, older, deactivated outfalls are permitted for use as temporary or emergency discharge locations; both discharge approximately 1 mile offshore, with the OCSD nearshore outfall at 20 m depth and the HTP outfall at 15 m depth (CRWQCB, 2010, 2012). Use of the nearshore outfalls for discharge diversion has been rare and recently limited to one event during 2006 when HTP performed an internal inspection of its standard pipe and one during 2012 when OCSD repaired its standard pipe. Additional diversions are possible in the future.

2. Model configuration

2.1. The ROMS model

The oceanic circulation model ROMS is used to simulate the circulation and tracer effluent dispersal in the coastal zone of Southern California. It includes K-Profile Parameterization (KPP; Large et al., 1994; Durski et al., 2004), a non-local turbulent closure model for vertical momentum and tracer mixing in the surface and bottom planetary boundary layers and in the interior of the fluid. In addition it has a numerical hyperdiffusion associated with horizontal advection with an effective diffusivity coefficient that decreases with the grid scale. The present ROMS configuration consists of quadruply nested model domains (Fig. 1) with an offline, one-way nesting technique that downscales from $dx=5$ km horizontal resolution of the U.S. West Coast (L0), to 1 km resolution for the Southern California Bight (L1), to 250 m resolution for the interior shallow area of the Bight with a multiple of large islands and deep basins (L2), and then to 75 m resolution for two separate subdomains encompassing Santa Monica Bay (L3a) and San Pedro Bay (L3b). Each domain has 40 (L0, L1, and L2) or 32 (L3a and L3b) topography-following levels vertically stretched such that grid cell refinement occurs most strongly near the surface and the bottom. The model topographies are from the 30 arcsec global bathymetry (SRTM30; Becker et al., 2009) overall, with refinement using the 3 s ($dx=90$ m) NOAA-NGDC coastal relief dataset[2] for the nearshore regions depending on data availability.

The outer L0 domain is forced by the monthly averaged data from SODA version 2.0.4, an assimilated global oceanic dataset (Carton and Giese, 2008) in the lateral boundary conditions; the monthly average AVHRR Pathfinder satellite sea surface temperature[3] (SST), and the COADS climatological dataset for sea surface salinity[4] (SSS). On the L0 grid the monthly climatology of runoff from major rivers (Dai and

[1] Buijsmann et al. (2012) use these same simulations to analyze the internal tide in the Southern California Bight.

[2] http://www.ngdc.noaa.gov/mgg/coastal/crm.html

[3] http://podaac.jpl.nasa.gov/DATA_PRODUCT/SST/index.html

[4] http://www.ncdc.noaa.gov/oa/climate/coads/

Trenberth, 2002) is included by addition to the surface freshwater flux. The intermediate L1 and L2 and the inner L3a and L3b grids are then driven by the corresponding parent ROMS model solutions with daily (L0 to L1) and 2-hourly (L1 to L2, L2 to L3a and L2 to L3b) lateral boundary updates. All the other surface boundary conditions such as momentum, heat, freshwater (evaporation minus precipitation), and radiation fluxes for all the ROMS models are given by an hourly atmospheric forcing by a double-nested Weather Research and Forecast model (WRF; Michalakes et al., 1998) with $dx=18$ and 6 km horizontal grids embedded in NCEP's North American Regional

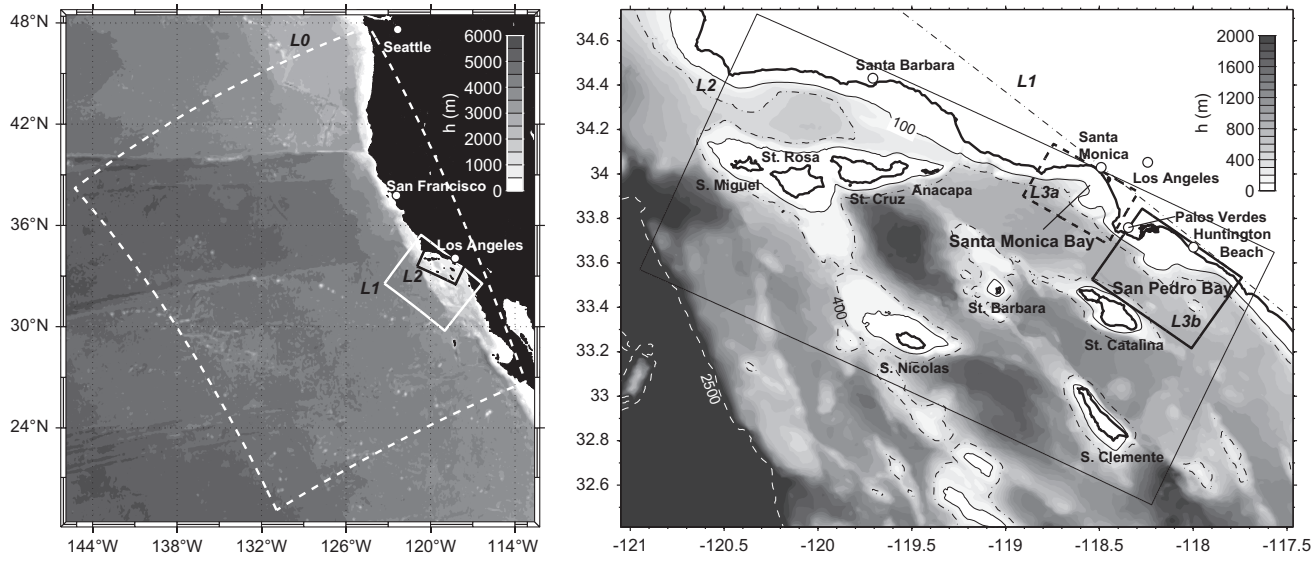

Fig. 1. The quadruply nested ROMS model domains and bathymetry [m] (gray scale). Left: three nested grids along the North American West Coast. The outer boundaries of the $dx=5$ km grid (L0), 1 km grid (L1), and 250 m grid (L2) are represented by the white dashed, white solid, and black solid lines. Right: Southern California Bight where the perimeters of the $dx=1$ km grid (L1), 250 m grid (L2), 75 m Santa Monica Bay grid (L3a), and 75 m San Pedro Bay grid (L3b) are represented by the thin dash-dot, thin solid, thick dashed, and thick solid rectangles, respectively. The 100, 400, and 2500 m isobaths are plotted with black solid, black dotted and white solid contours to indicate mainland/island shelves and continental shelf breaks.

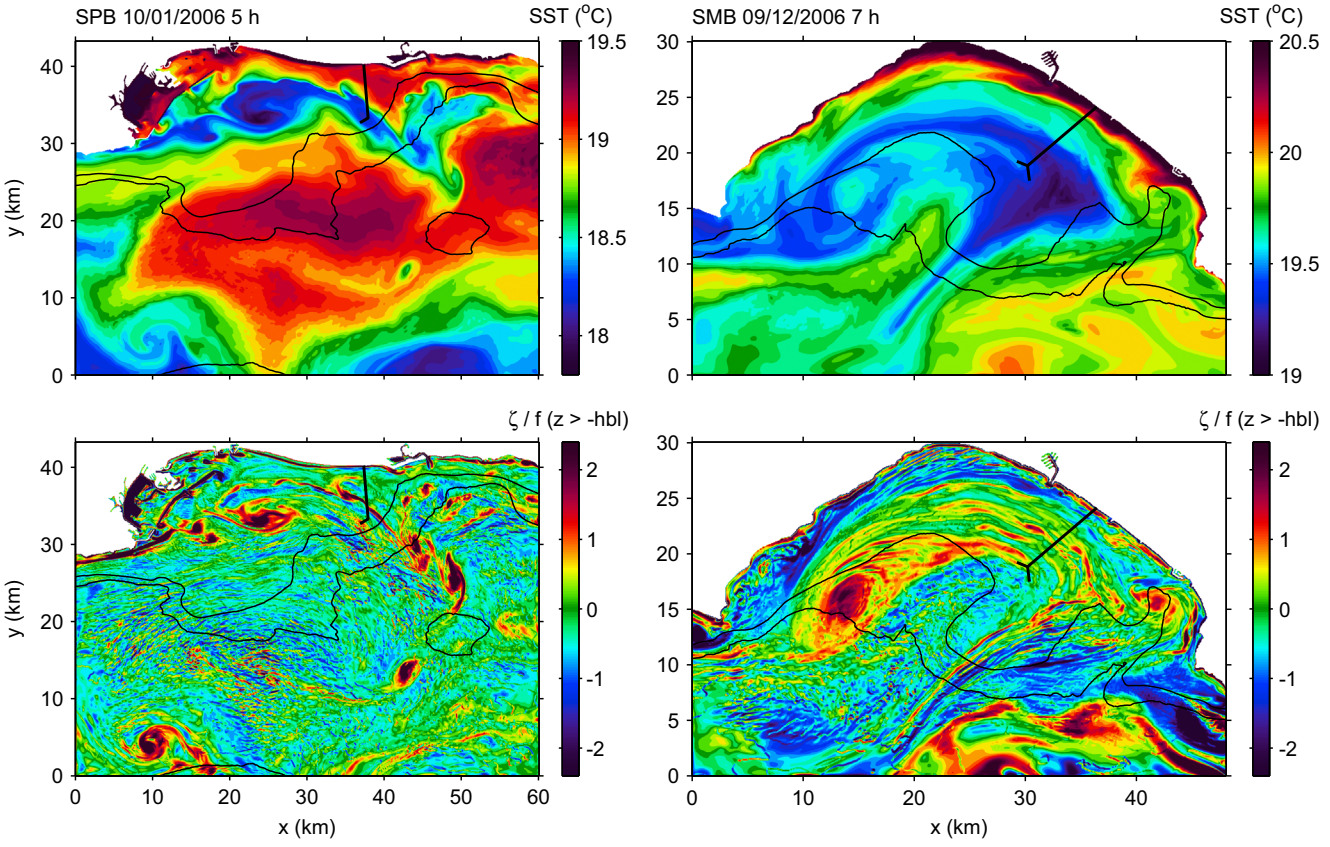

Fig. 2. Instantaneous fields of surface temperature (SST; top row) [C] and vertical vorticity ζ averaged over the surface boundary layer and normalized by the Coriolis frequency $f=0.8\times10^{-4}\ s^{-1}$ (bottom). The left column is SPB on October 1, 2006, and the right column is SMB on September 12, 2006. The locations of the outfall pipes are indicated by the black lines.

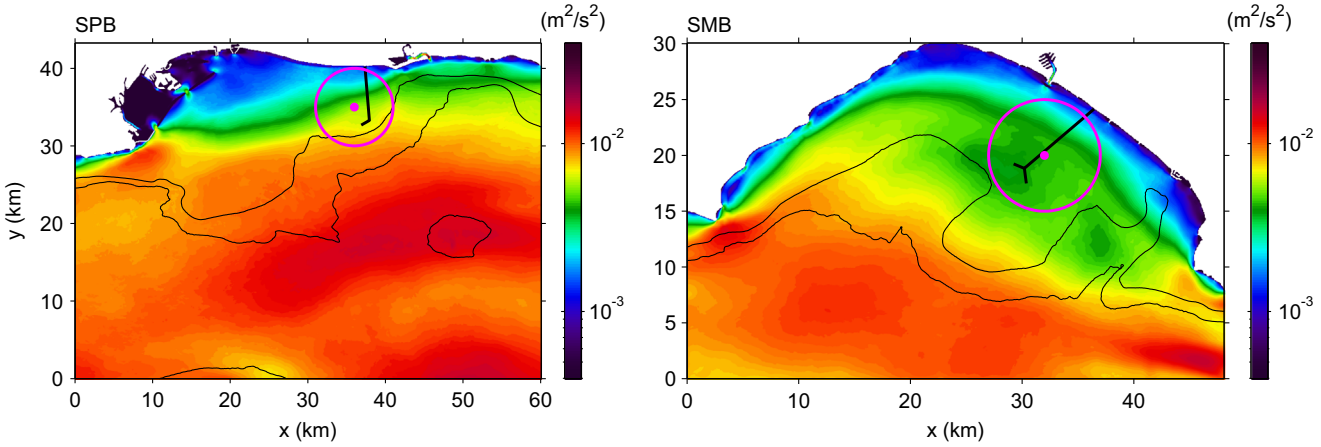

Fig. 3. Surface, subseasonal eddy kinetic energy [$m^2\,s^{-2}$] in SPB (left column) and SMB (right). Magenta circles are the areas with a diameter of 10 km for the spatial averaging used for Table 1 (Section 3). (For interpretation of the references to color in this figure caption, the reader is referred to the web version of this paper.)

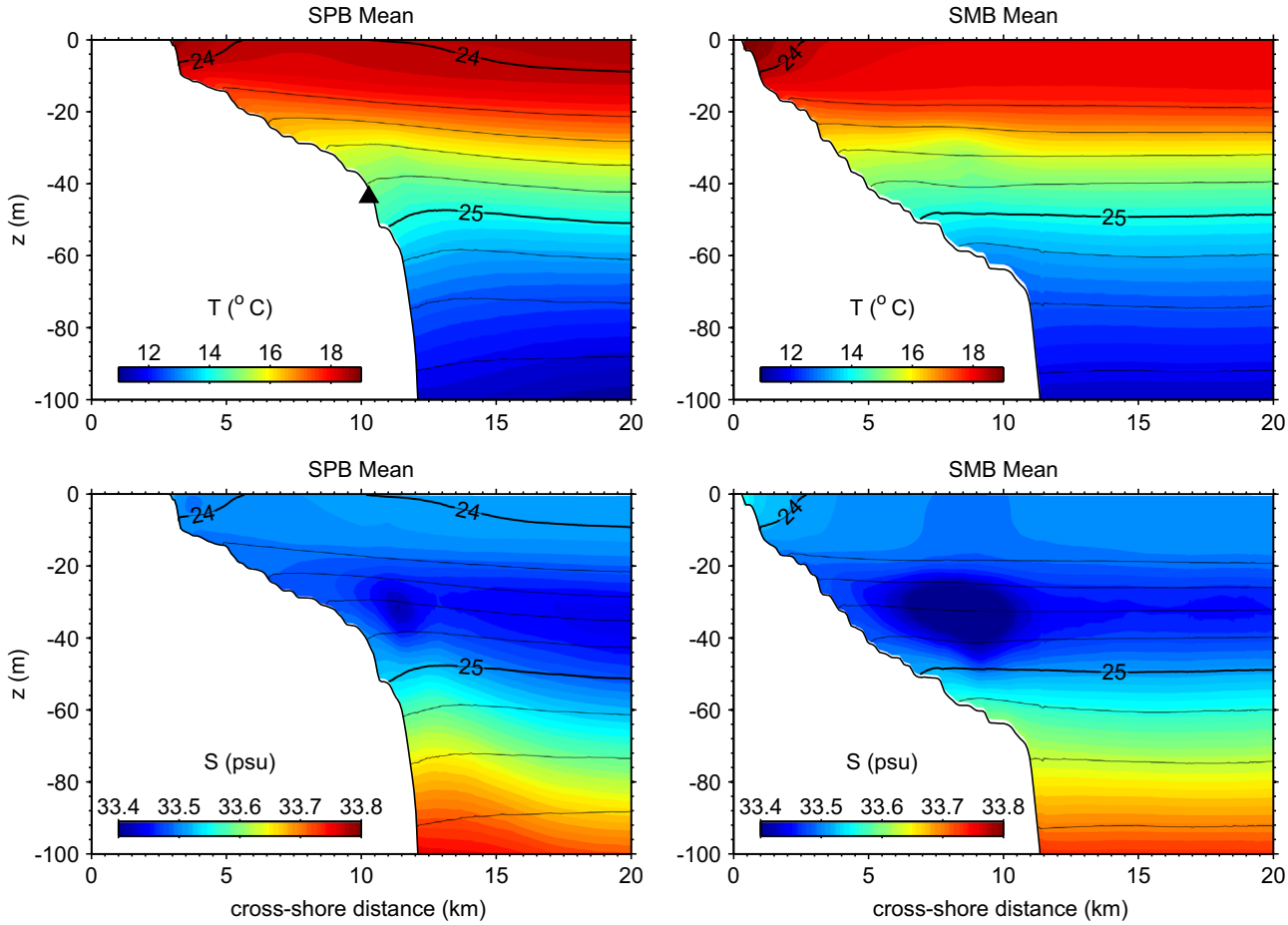

Fig. 4. Time-mean $T(x,z)$ [C] and $S(x,z)$ [PSU] along sections parallel to the outfall pipes in SPB (left column) and SMB (right column) (see Fig. 8). Black contours and labels show σ, the density excess over 10^3 kg m^{-3}. These fields are for the simulations with standard outfalls. Black triangles indicate the approximate locations of the outfall diffusers.

Reanalysis with a 32 km horizontal grid.[5] The 18 km WRF solution is used to force the ROMS L0 model, while the 6 km solution is used for the L1, L2, L3a and L3b models with a one-way coupling approach. The full nested sequence from L0 down to L3 is run for the primary simulation period of August 1–November 30, 2006. Prior to this the L0 model is spun up for many years with climatological surface forcing, and then a synoptic spin up run is made for L0 with QuikSCAT-ECMWF blended winds[6] for 2004–2006, with shorter nested spin up periods for L1 (8 months) and L2 (1 month). At each stage the finer-grid fields are initialized with the coarser-grid fields.

[5] http://www.emc.ncep.noaa.gov/mmb/rreanl/

[6] http://cersat.ifremer.fr/Data/Discovery/By-product-type/Gridded-products/MWF-Blended

The L1 domain is forced at its lateral boundaries with water level and barotropic current amplitudes, and phases for ten tidal constituents (i.e., M_2, S_2, N_2, K_2, K_1, O_1, P_1, Q_1, M_f, and M_m). The amplitudes and phases are synthesized with the corresponding tidal constituents from the TPXO 7.1 global tidal prediction model (Egbert et al., 1994). At every baroclinic time step, the tidal water level and velocities are superposed on the daily-averaged boundary conditions from the L0 run. The full three-dimensional variability in L1 is projected onto the L2 boundaries by an update every 2 h, and the same approach is taken from L2 to L3a and L3b. An extensive model-data comparison has been made in a non-tidal configuration similar to L1 by Dong et al. (2009), and Buijsmann et al. (2012) assessed barotropic and baroclinic tides in the Bight in the L2 and L3 solutions; both of these validation assessments show fair quantitative agreement.

2.2. Effluent tracer source

Given an input pollutant concentration in the outfall pipe $\mathcal{C}_p$ [kg/m^3] with volume flux $\mathcal{Q}_p(t)$ [m^3/s], we force a nondimensional tracer concentration equation by an equivalent source $\mathcal{P}$ [1/s]

$$\frac{\partial c}{\partial t} = -\nabla \cdot \mathbf{F} + \mathcal{P}, \tag{1}$$

with

$$\mathcal{P}(x,y,z,t) = \mathcal{P}_s(t)\mathcal{A}(x,y)\mathcal{H}(z), \tag{2}$$

here c is pollutant concentration normalized by $\mathcal{C}_p$ (unlike salinity, which is a mass fraction of seawater), and $\mathbf{F} = \mathbf{u}c + \mathbf{F}_{sgs}$ is the advection-mixing flux associated with the resolved flow and the subgrid-scale (*sgs*) parameterizations (Section 2.1). $\mathcal{A}$ and $\mathcal{H}$ are the specified spatial functions mimicking the outcome of unresolved nearfield mixing above the outfall diffusers; their values are non-dimensional and close to one in the source region and zero outside it. They have integrals equal to the effective source area and depth

$$\iint \mathcal{A}\, dx\, dy = A_s, \quad \int \mathcal{H}\, dz = H_s, \tag{3}$$

Table 1
Velocity vector magnitude [10^{-2} m s^{-1}] in temporal–spatial bands: the time mean speed and the fluctuation RMS for mesoscale (period P=30 h–90 days; horizontal wavelength L > 20 km), submesoscale (P=30 h–90 days; L < 20 km), diurnal (P=18–30 h), and semidiurnal (P=8–18 h) bands. Averages are made within a circle of diameter 10 km centered 2 km inshore from the outfall. Separate averages are made for two depth intervals: surface ($z \geq -h_{bl}$) and subsurface $-\min[\text{h},\ 75\ \text{m}] \leq z < -h_{bl}$).

	San Pedro Bay		Santa Monica Bay	
component	Surface	Subsurface	Surface	Subsurface
Mean	3.37	5.72	1.32	0.12
Mesoscale	7.80	4.80	5.06	3.18
Submesoscale	4.55	3.41	5.10	3.53
Diurnal	2.75	1.37	2.87	1.35
Semidiurnal	2.84	2.11	2.56	1.59

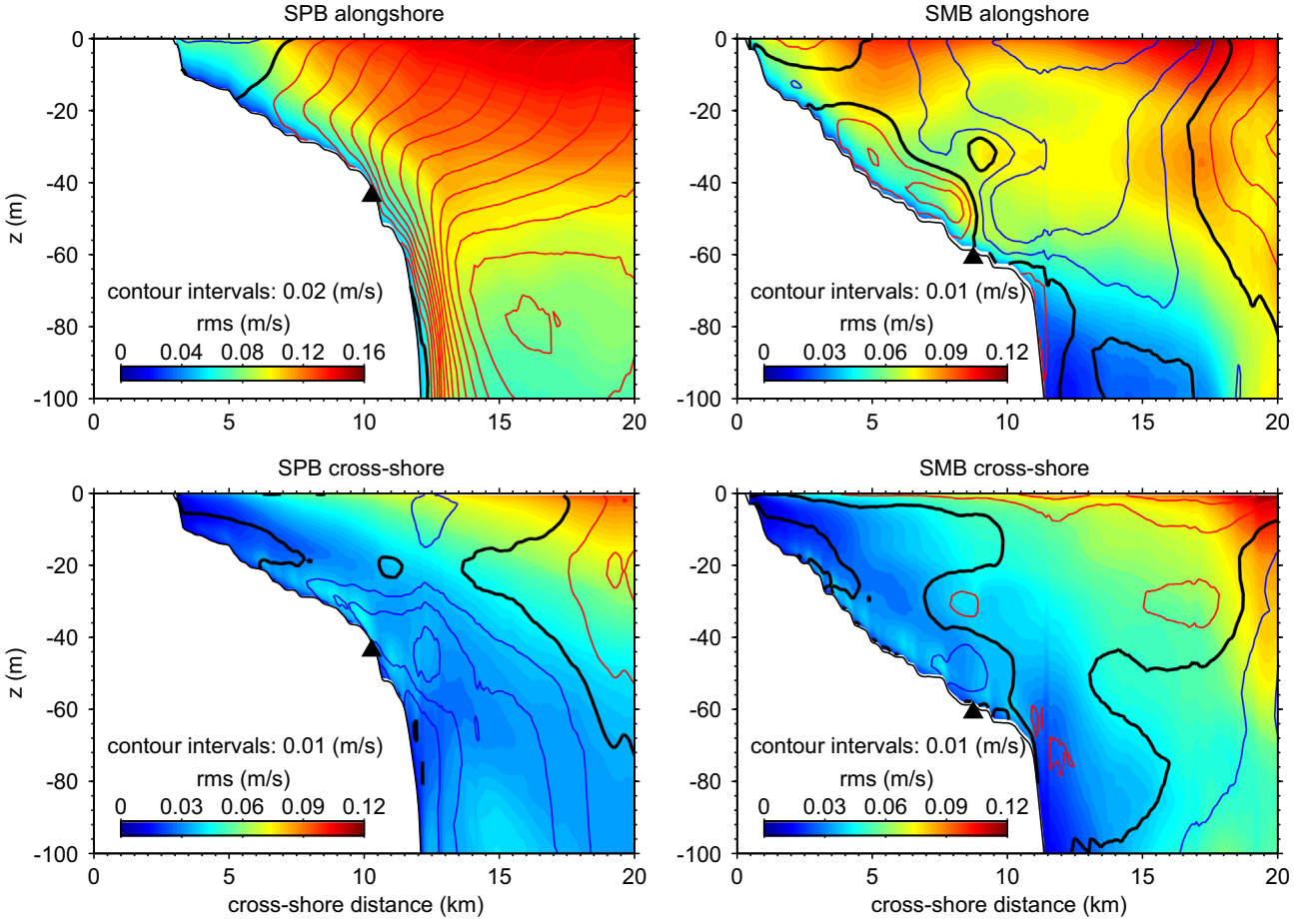

Fig. 5. Cross-shore sections of velocity mean (contours) and subseasonal fluctuation root-mean-square (RMS; colors) [m s^{-1}]. The sections parallel the outfall pipes in SPB (left column) and SMB (right column). The velocity vector is decomposed into its poleward alongshore component (top row) and shoreward cross-shore component (bottom row). The heavy solid line is the zero contour, and the thin red and blue solid lines are, respectively, positive and negative contours with the indicated intervals (0.01 or 0.02 m/s). Black triangles indicate the approximate locations of the outfall diffusers. (For interpretation of the references to color in this figure caption, the reader is referred to the web version of this paper.)

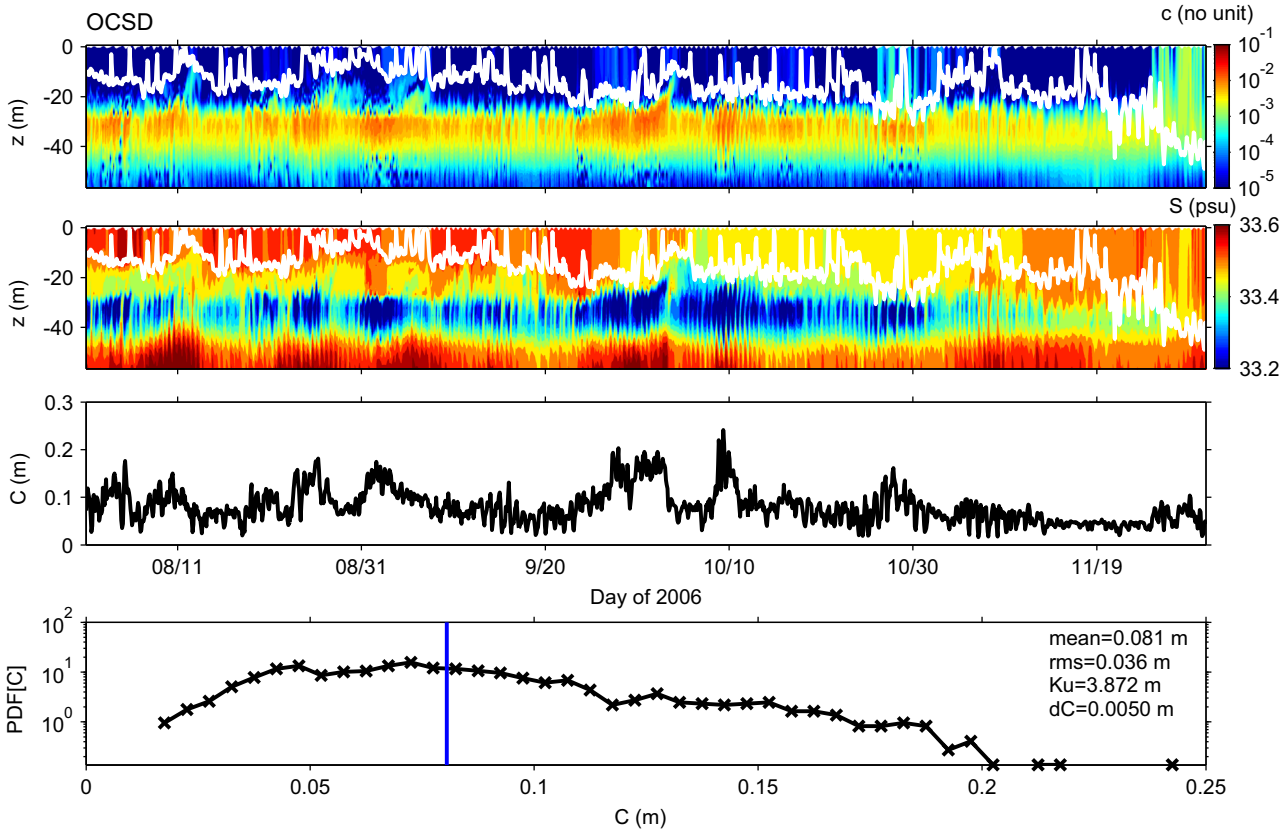

Fig. 6. Time series of the normalized tracer concentration $c(z,t)$, salinity $S(z,t)$, vertically integrated normalized tracer concentration $C(t)$, and the probability density function $P[C]$ for the average of the $N_s=23$ model grid points used as the standard outfall effluent source region of OCSD. c and S plots also show the surface turbulent boundary layer depth, $z=-h_{bl}$ (white line). In the bottom panel the bin size for $P[C]$ is $dC=0.005$ m, with normalization $\sum_i P[C_i]\,dC=1$. The mean of $C(t)$ is demarcated by the blue vertical line and its value is listed along with the root-mean square (RMS) and kurtosis (Ku) for C fluctuations relative to the mean. S plots show mid-depth salinity minima that have been frequently observed in the area (*e.g.*, Todd et al., 2009, Fig. 10), augmented by the effluent freshness. (For interpretation of the references to color in this figure caption, the reader is referred to the web version of this paper.)

with A_s the horizontal area, H_s the vertical size, and $V_s=A_sH_s$ the volume. $\mathcal{P}_s$ is determined from integrated tracer equivalence between the model source and the pipe inflow by the relation, $\mathcal{P}_s=\mathcal{Q}_p/V_s$. For our simulations we use outfall data for $\mathcal{Q}_p(t)$. To translate from our c fields for any particular pollutant species (*e.g.*, CDOM), we could multiply by its inflow concentration value $\mathcal{C}_p$. Because the vertical structure of c is relatively simple compared to its (x,y,t) structure, we define the vertically integrated, normalized tracer by

$$C=\int c\,dz; \tag{4}$$

its unit is m. There is an analogous forcing source in the model's salinity S equation, $\mathcal{R}=\mathcal{R}_s\mathcal{A}\mathcal{H}$, by the freshwater flow out of the pipe, where integral balance implies that $\mathcal{R}_s=-S_o\mathcal{Q}_p/V_s$ with $S_o=35$ PSU, the mean oceanic salinity.

The wastewater effluents are specified as monthly-averaged freshwater volume fluxes of $\mathcal{Q}_p=5.4$–6.2 m^3/s smoothly interpolated in time for OCSD and a constant 15.3 m^3/s for HTP; these values are not precisely accurate for Fall 2006, but are representative of the discharges.[7] Daily-averaged discharge of the three local rivers (Los Angeles River, San Gabriel River, and Santa Ana River) are included as freshwater volume fluxes at the corresponding mouth locations, although the model indicates that their influence is minor in Fall 2006, and they will not be discussed here. The nearfield vertical mixing of the buoyant effluent occurs on a scale smaller than our grid resolution, and, as a hydrostatic model, ROMS is ill-suited for the large local vertical velocities associated with the freshwater discharge from the bottom-mounted pipes. Therefore, we specify the outcome of the nearfield initial mixing and dilution by imposing the prescribed spatial distributions of $\mathcal{A}$ and $\mathcal{H}$ in (2).

$\mathcal{A}=1$ in the horizontal grid cells that tile the diffuser pipe segment, and it is zero elsewhere. So $A_s=N_s\,dx^2$, where N_s is the number of tiling cells and $dx^2=5.6\times10^3$ m^2 is the cell area. For OCSD $N_s=23$ for the 5-mile outfall pipe, and $N_s=12$ for the 1-mile pipe; for HTP $N_s=32$ for the 5-mile pipe, and $A_s\approx dx^2$ for the 1-mile pipe (which lacks a diffuser). We fit a Gaussian shape function to $\mathcal{H}$ with parameters guided by nearfield buoyant plume solutions obtained by OCSD using the model of Roberts et al. (1989) with measured currents near the outfall:

$$\mathcal{H}(z)=\exp\{-(z-z_s)^2/d_s^2\}. \tag{5}$$

z_s is the plume center height and d_s is its vertical scale. A half-space integral of this $\mathcal{H}(z)$ is $0.5\sqrt{\pi}d_s$. For the 5-mile outfalls, we choose $z_s=-h+20$ m (with h being the bathymetric depth) and $d_s=7.1$ m, hence $H_s=\sqrt{\pi}d_s=12.5$ m (neglecting top and bottom boundary limits to the integral). This $\mathcal{H}(z)$ does not reach the surface due to density stratification in the pycnoline. For the 1-mile outfalls, the plume penetrates the stratification and rises up to the surface: $z_s=0$. We further choose $d_s=10$ m, hence $H_s=8.9$ m neglecting the bottom boundary limit.

A feasible future generalization of this nearly steady effluent source is to use monitored $\mathcal{Q}_p(t)$ and run the nearfield buoyant plume model with modeled local currents. This would contribute

[7] The effluent concentrations linearly scale with $\mathcal{Q}_p$, apart from the additional dynamical forcing by $\mathcal{R}$, which has modest nonlinear effects in our simulations.

additional source variability to the effluent distributions seen in the present solutions (Sections 4 and 5), and it would more consistently determine the nearfield plume dilution rates in response to local ambient conditions. However, we have specified the model source with a fixed mixing volume, $\int \mathcal{AH}\, d\mathbf{x}$, to represent the nearfield plume dilution, whereas in nature the mixing volume may vary; this bias is difficult to remedy in a fixed-grid model even with the very fine dx employed here. Furthermore, there is an issue whether the assumed scale separation between the calculated variable circulation and concentration and the parameterized nearfield plume mixing is valid; for fine enough model resolution this assumption will fail, and the turbulence of the plume must be calculated explicitly (*e.g.*, as in Weil et al., 2012, for an atmospheric convective regime).

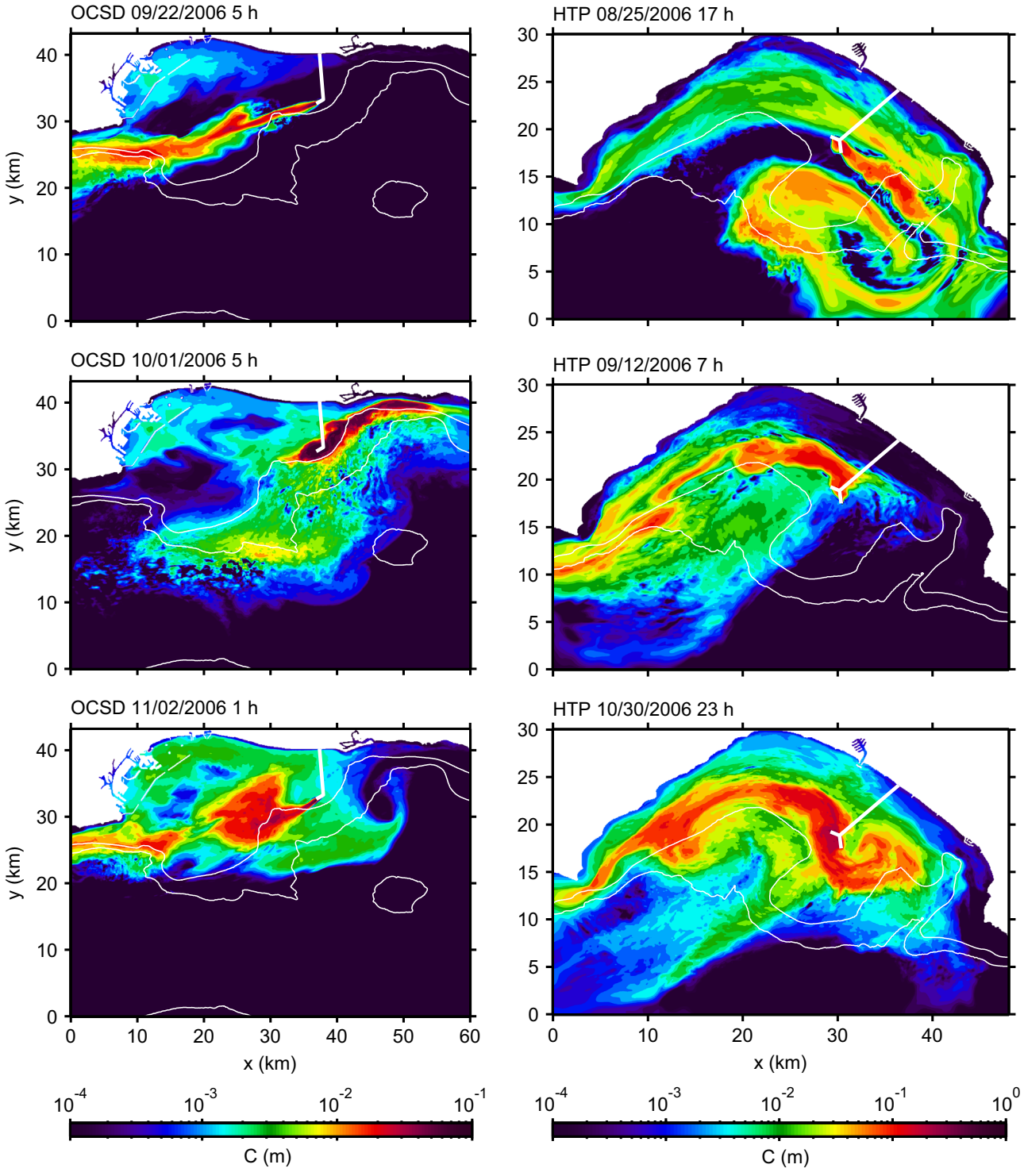

Fig. 7. Snapshots of representative patterns of $C(x, y)$ for OCSD (left column) and for HTP (right). Thick white lines indicate standard outfall pipes, and light white lines are the 100 and 500 m isobaths. Axis distances are in km. The middle-row times are the same as in Fig. 2.

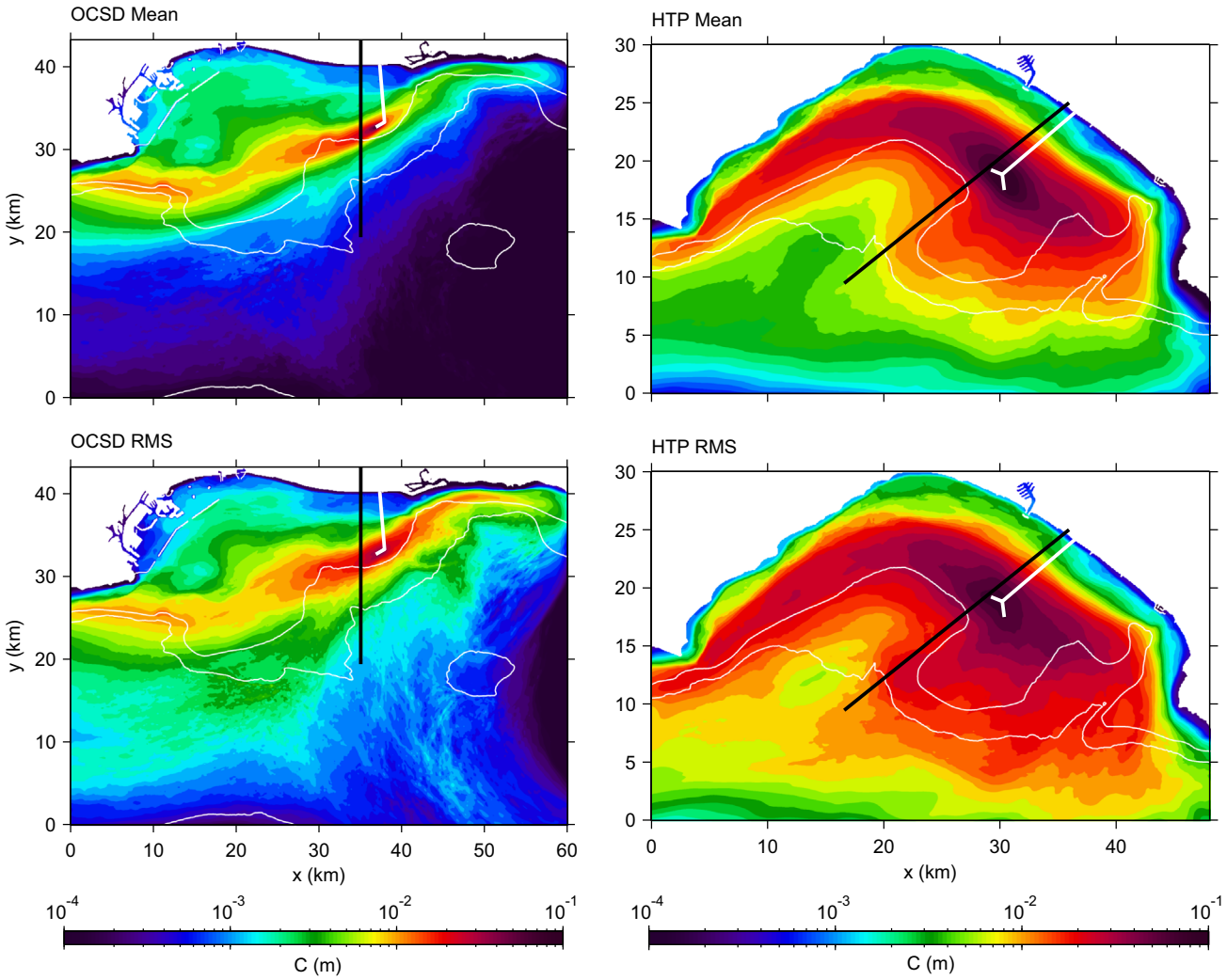

Fig. 8. Mean and RMS of $C(x,y,t)$ for OCSD (left column) and HTP (right). White lines are outfall pipes, and black lines indicate the cross-sections in Fig. 9.

3. Currents and stratification

The primary circulation pattern in the Bight is the surface southward flow of the California Current offshore and the poleward California Undercurrent adjacent to the continental slope (Dong et al., 2009). Within SPB and SMB the transient flow is dominated by eddies and tides. Illustrative patterns for surface temperature (SST) and vertical vorticity ζ are in Fig. 2. The horizontal scale in SST is larger than in ζ. We interpret the former as more indicative of mesoscale eddies with a size of tens of km or more, whereas ζ shows submesoscale vortices and filaments with a size of a few km. These mesoscale and submesoscale structures are ubiquitous in SPB and SMB according to the satellite and radar observations (*e.g.*, Di Giacomo and Holt, 2001; Bassin et al., 2005), known as "spiral eddies". The observed submesoscale eddies are 4–15 km in diameter and typically persist for several days. SPB typically has warmer water supplied from the south, while SMB has cooler water partly supplied from the north. Both bays exhibit a narrow coastal strip (<5 km wide) of warmer water, as a result of local heating.

We define the eddy kinetic energy, $\mathbf{u}'^2/2$, using the horizontal velocity $\mathbf{u}'$ extracted with a high-pass temporal filter retaining fluctuation periods $P<90$ days (*i.e.*, including all subseasonal time scales). Its spatial distribution (Fig. 3) shows a systematic decrease from the offshore region outside the bays to the coastal strip that is roughly coincident with the warm SST. Eddies are weaker within the bays due to both headland sheltering and enhanced dissipation by bottom drag in shallow nearshore water. The outfalls are in the middle of the continental shelves in an intermediate energy zone. SPB has a narrow shelf on its southeast side, and its outfall site is exposed to greater eddy activity than in SMB. This is the first of several indications that effluent dispersal is more efficient for OCSD than for HTP.

The water in the bays is well stratified in both T and S (Fig. 4). T is the dominant influence on density σ. The thermocline is shallow and thin, spanning the depth range from the bottom of the surface boundary layer at $z=-h_{bl}$ (determined as part of the KPP vertical mixing scheme) down to about 70 m. Thus, the standard outfalls are in the lower thermocline, while the nearshore diversion pipes are in very weakly stratified water (even without the destabilization by the buoyant effluent plume). S has a mid-depth minimum in the thermocline. It exhibits fresh anomalies just above the standard outfalls due to the effluent plumes. The S anomaly is much larger in SMB (>0.1 PSU) than SPB, due to both its higher inflow rate $\mathcal{Q}_p$ (Section 2.2) and its less efficient dispersal.

Fig. 5 is the time-mean velocity and root-mean-square (RMS) subseasonal variability in cross-shore sections parallel to the outfall pipes. The mean flow in SPB is a strong, poleward alongshore California Undercurrent with a peak speed of 0.3 m s^{-1} located over the continental slope about 5 km offshore

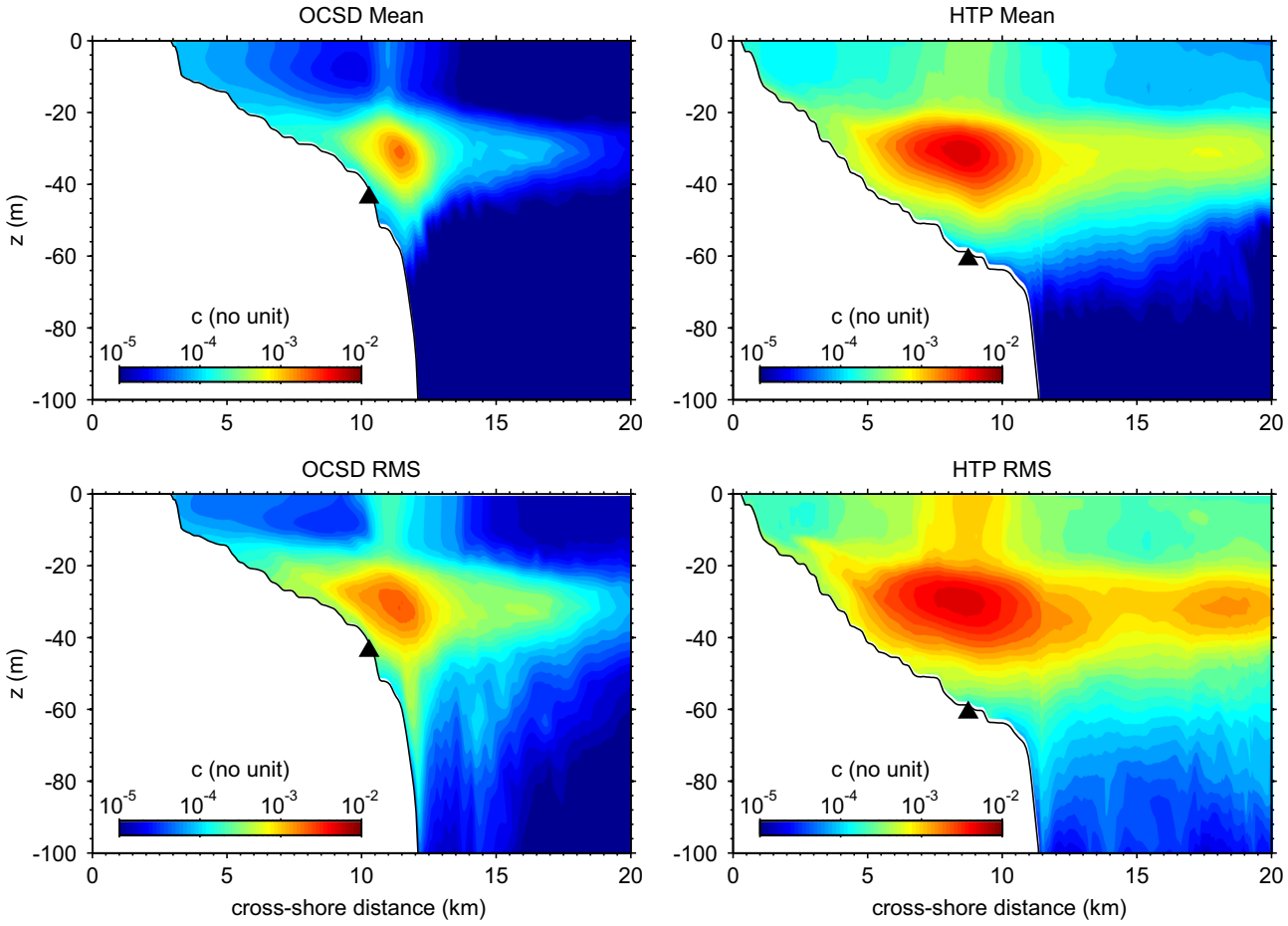

Fig. 9. Mean and RMS of $c(z,x,t)$ for OCSD (left column) and HTP (right) in the vertical cross-sections indicated by the black lines in Fig. 8. Black triangles indicate the approximate locations of the outfall diffusers.

from the outfall.[8] In contrast, the alongshore mean flow in SMB is quite weak, and its Undercurrent is much farther offshore. The cross-shore mean flows are weak in both bays. The alongshore and cross-shore variability levels are similar offshore of both bays (~ 0.1 m s^{-1}). They both decrease approaching the shoreline, much more rapidly in the cross-shore component. There is also a moderate decrease with depth in both components in both bays. Therefore, we expect effluent dispersal to be primarily alongshore, with an appreciable mean displacement to the northwest in SPB.

A low-pass frequency Butterworth filter is adapted to decompose the velocity field into seasonal (the period band $P \geq 90$ days, simply called time-mean) and subseasonal ($P < 90$ days) currents (Fig. 3). The latter is further decomposed into eddy (30 h $< P \leq 90$ days), two tidal (diurnal band: 18 h $< P \leq 30$ h, and semi-diurnal band: 8 h $< P \leq 18$ h), and turbulent ($P \leq 8$ h) components. Then we make use of a Gaussian spatial filter to the eddy component to extract mesoscale (the wavelength $L > 20$ km) and submesoscale ($L < 20$ km) fluctuations. Finally, we separate the currents into a surface layer average over the boundary layer, and subsurface average over the interval below the boundary layer down to the shallower of either the bottom depth or the thermocline base (75 m). (The subsurface layer contains the bulk of the near-field plume from the standard outfalls.) Statistical averages are made in time (August 15–November 30, 2006) and over a circular area with a 10 km diameter containing the standard outfalls (magenta circles in Fig. 3). The resultant velocity magnitudes are summarized in Table 1. It is remarkable how all the flow components contribute similarly in magnitude. The mean (in SPB) and eddies do dominate the tides. Tidal parcel displacements, $\ell_{max} = PU_{rms}/\sqrt{2}\pi$, are typically less than 1 km for both bands, which means that they are inefficient as dispersal agents. The mesoscale eddies have slightly stronger RMS velocity magnitude than the submesoscale eddies in SPB, but the reverse is true in SMB. Their displacements are much larger because of their longer persistence (especially mesoscale).

With the same time and area averaging procedure, we determine the RMS vertical vorticity ζ to be $0.72f$ and $0.75f$ for SPB surface and subsurface layers and $0.82f$ and $0.57f$ for SMB surface and subsurface layers, respectively. This quantity is dominated by the submesoscale eddies (evident in Fig. 2, right), and they also dominate the process of increasing tracer gradient through straining deformation. Vertical vorticity ζ and the horizontal strain rate α have equal RMS values in a non-divergent flow in a homogeneous domain,[9] so we can estimate α by RMS ζ. Advection by a

[8] This poleward mean flow on the San Pedro slope is roughly consistent with the velocity measurements in Noble et al. (2009a; Figs. 4 and 5) and with the modeled mean subsurface flow pattern in Dong et al. (2009; Fig. 6). However, the measurements also show that there can be considerable variation among currents averaged over a single season, as here; Hamilton et al. (2006, Fig. 5) shows a relatively stronger equatorward surface flow on the shelf during summer, 2001, than that in Fig. 5.

[9] For a non-divergent horizontal flow, $u = -\partial_y\psi$, $v = \partial_x\psi$ with ψ the stream-function, $\zeta = \partial_x v - \partial_y u = \partial_{xx}\psi + \partial_{yy}\psi$, and $\alpha^2 = (\partial_x u - \partial_y v)^2 + (\partial_y u + \partial_x v)^2 = (\partial_{xx}\psi - \partial_{yy}\psi)^2 + 4(\partial_{xy}\psi)^2$ is the squared magnitude of the two independent components of the strain rate tensor. The variance difference $\zeta^2 - \alpha^2 = 4(\partial_{xx}\psi\partial_{yy}\psi - (\partial_{xy}\psi)^2)$ vanishes in an area integral, as seen by integration by parts in x and y assuming no boundary integral contributions by the homogeneity assumption (*e.g.*, equivalent to spatial periodicity).

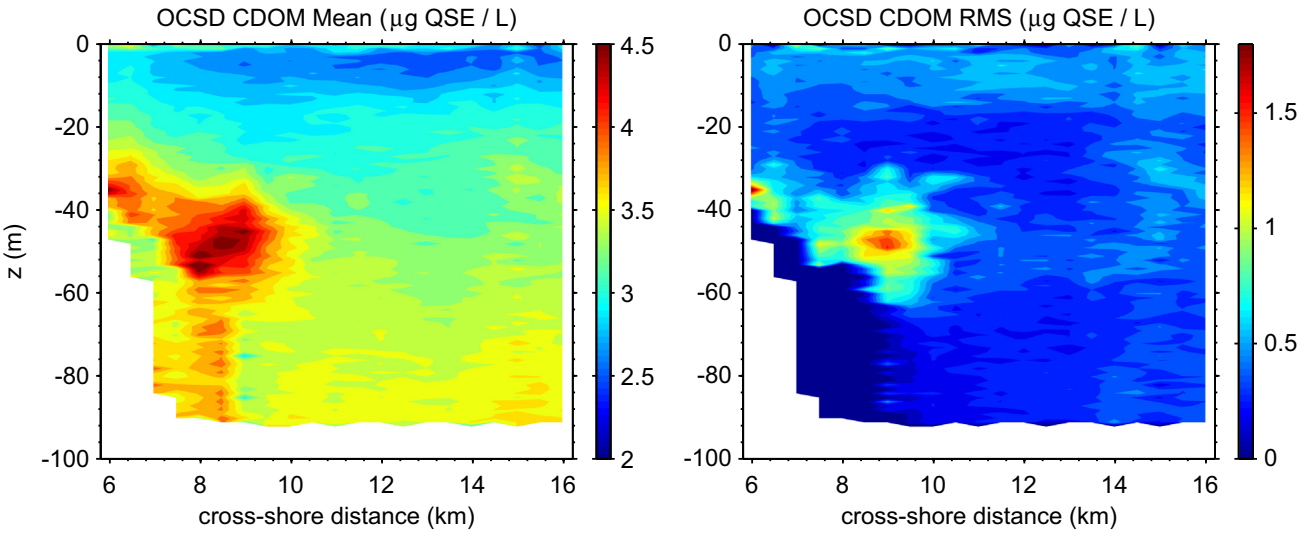

Fig. 10. Mean and RMS of CDOM in μg QSE l^{-1} in SPB measured by a glider along a transect about 2 km east of the transect in Fig. 8. QSE stands for quinone sulcate equivalents. The glider measurement was conducted repeatedly from March 3, 2010 till June 17, 2010. (Courtesy of Burton Jones of University of Southern California.)

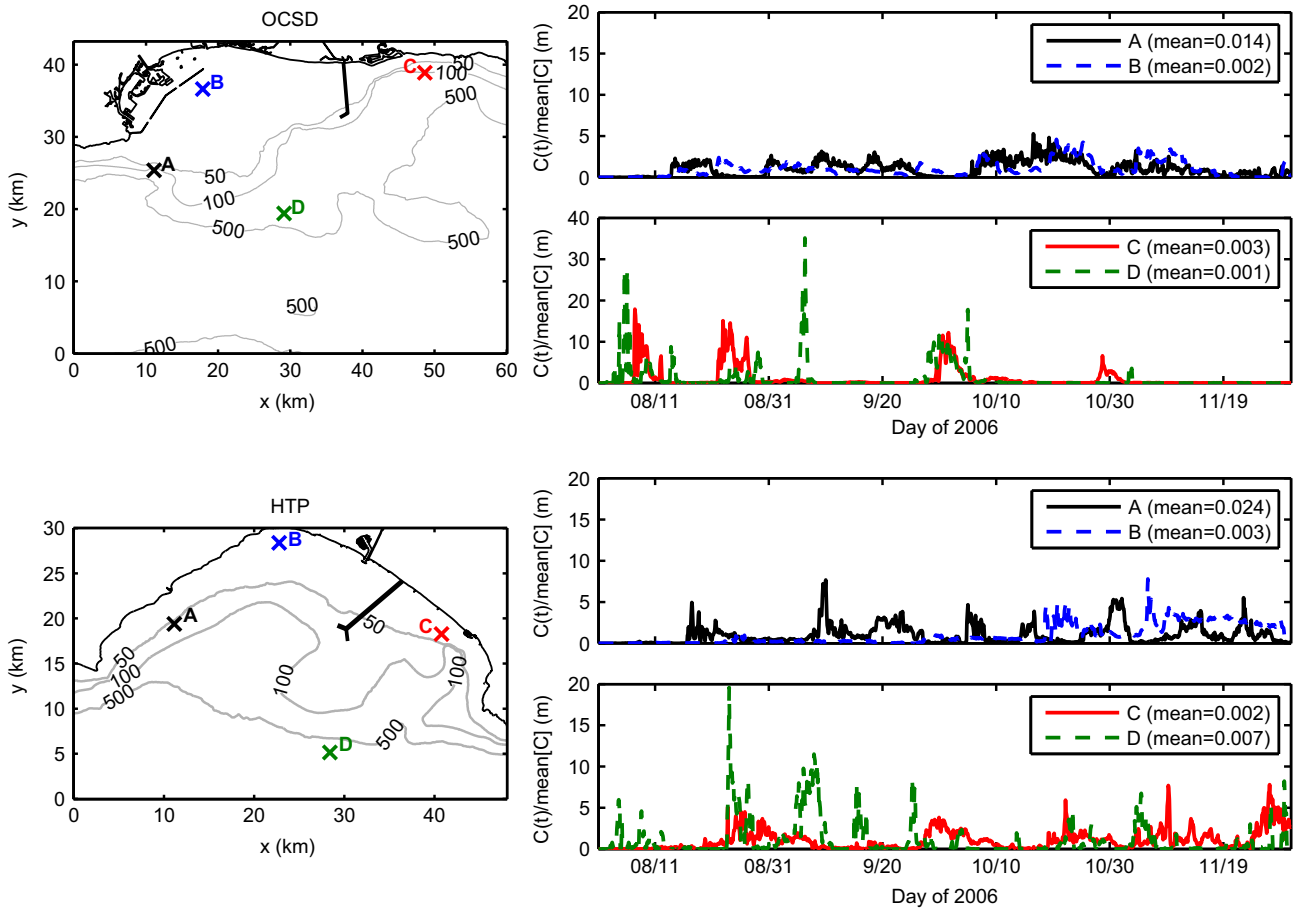

Fig. 11. Point time series of $C(t)$ [m] in OCSD (upper panels) and HTP (lower panels). Point locations are indicated on the maps in the left columns, along with the outfall pipes and the 50, 100, and 500 m isobaths. The time series are normalized by the local time mean, listed in the panel.

pure strain flow acts to decrease the horizontal scale of a tracer field exponentially quickly, *i.e.*, $\ell \sim \ell_0 \exp[-\alpha t]$. Hence, we estimate a typical dilution time for a tracer patch of size ℓ_0 to reach the grid scale dx where model diffusion acts by $\log[\ell_0/dx]/\alpha$, which has an approximate value of 1 day near the outfalls. Mesoscale velocities are comparable to the submesoscale ones (Table 1), but their strain rates are larger because their horizontal scale is larger; thus, mesoscale dilution rates are slower than submesoscale ones. We see the effects of both in the tracer effluent patterns in the next section.

4. Effluent distribution: standard outfalls

The modeled response in the source region above the OCSD outfall diffuser pipe is shown in Fig. 6. The concentration $c(z,t)$ is largest in the depth range of $\mathcal{H}(z)$, and the vertical structure is not highly variable except for episodic intrusions into the surface layer (*e.g.*, during the stormy period in late November when the boundary layer rapidly deepens). Both c and C vary much more in time than does $\mathcal{Q}_p$. This is due to large variations in **F** associated with local current fluctuations **u**. The peak value of nearfield $c(z,t)$ is 0.021, which is consistent with the assessment in the OCSD (2012) report. (The corresponding peak nearfield value for HTP is 0.022, consistent with the assessment in City of Los Angeles, 2007.) The integrated content $C(t)$ varies by about a factor of ten in its extremes, and it shows time scales that are mesoscale (weeks), submesoscale (days), and tidal (semidiurnal and diurnal). The tidally induced fluctuations are small compared to the eddy ones. The mean value of C is larger here than the RMS of the fluctuations around it. The probability density function (PDF) for C, $P[C]$, has a broad distribution with an approximately exponential shape to the tail, $P \sim \exp[-\gamma C]$ for some constant γ; this indicates intermittent occurrence of relatively high concentration compared to a normal distribution, although the kurtosis value ($Ku[C] = 3.9$, the normalized fourth moment of fluctuations about the mean of C) is only moderately large at the outfall because of the nearly constant inflow. The source-region salinity profile $S(z,t)$ shows a fresh anomaly that largely mirrors the $c(z,t)$ variations.

We estimate an approximate value for the source region concentration $\tilde{c}_s$ assuming a source inflow $\tilde{\mathcal{Q}}_p$ and a typical advection velocity $\tilde{u}_s$. A volume integral over the source region and quasi-steady balance in the tracer Eq. (1) is a balance between the total source, $\mathcal{P}_s V_s = \tilde{\mathcal{Q}}_p$, and the advective flux through a side

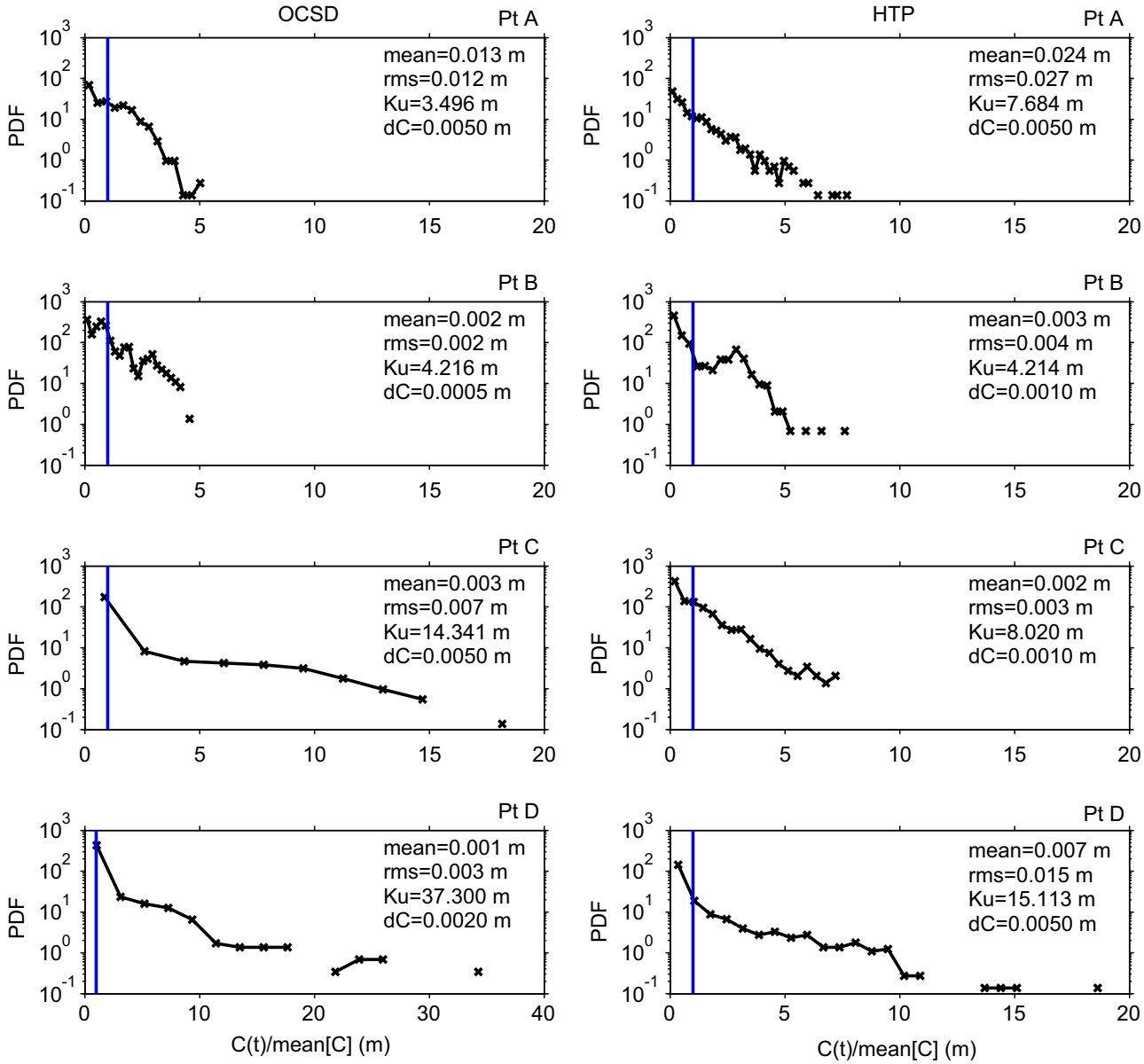

Fig. 12. PDFs $P[C]$ for the average of the nine model grid points around the point locations indicated in Fig. 11: OCSD (left column) and HTP (right). The bin size for each $P[C]$ is listed, and the mean of $C(t)$ is plotted with a blue line ($=1$ on the normalized abscissa) and is listed along with the RMS and Ku values for C fluctuations about the mean.

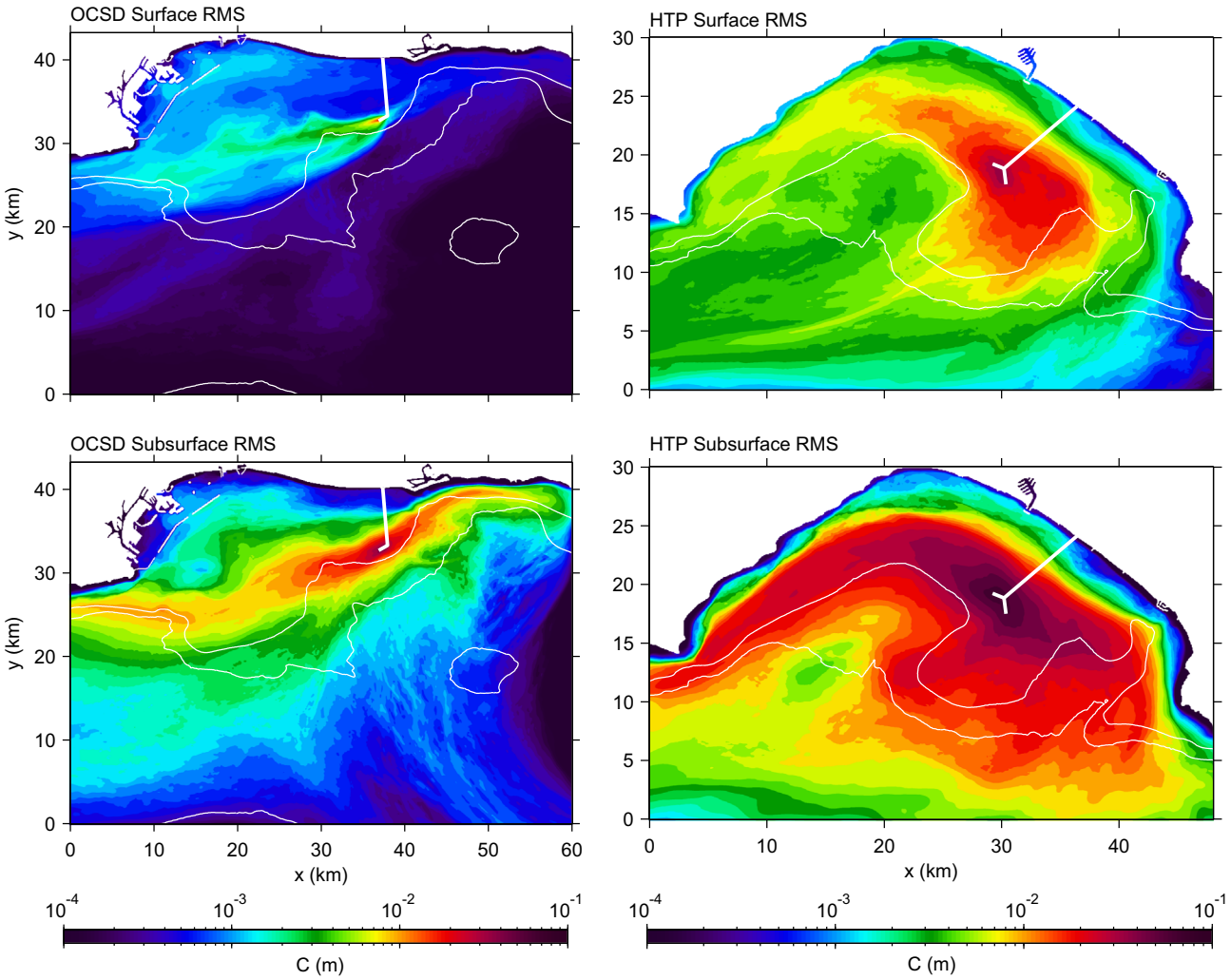

Fig. 13. RMS of $C(x,y,t)$ vertically integrated over the surface layer, defined as between the water surface and the bottom of the surface boundary layer (upper row), and over the subsurface layer, defined as between the bottom of the boundary layer and the shallower of either the bottom depth or 75 m (lower): OCSD (left column) and HTP (right).

section, $\tilde{u}_s H_s L_s \tilde{c}_s$, with L_s a typical section width in the near field, assuming that there is no influx from the upstream side

$$\tilde{c}_s = \frac{\tilde{Q}_p}{H_s L_s \tilde{u}_s}. \tag{6}$$

This is only a rough interpretive relation because even the mean of **F** is not just uniform advection. Nevertheless, for the OCSD values of $\tilde{Q}_p \approx 5\ \mathrm{m^3\ s^{-1}}$, $H_s \approx 10$ m, $L_s \approx 500$ m, and $\tilde{u}_s \approx 0.1$ m/s (*cf.*, Section 2.2, Table 1 for RMS subsurface velocity, and Fig. 7 for initial plume width), we obtain $\tilde{c}_s \approx 10^{-2}$ and $\tilde{C}_s = \tilde{c}_s H_s \approx 0.1$ m, which are consistent with the top and bottom panels in Fig. 6.

Instantaneous effluent patterns are highly variable (Fig. 7). At times the lateral plume moving away from the source is coherent over tens of km, but other times it folds back on itself due to eddy current reversals. Tracer movement is usually more alongshore than cross-shore. Mostly the tracer stays on the continental shelf, and excursions beyond the continental slope are rare. Hence C is small in the open sea. Dilution is evidently occurring because the patterns of previously emitted effluents are erased approximately on a mesoscale length as large as the width of the bays and a time scale of about a week (Fig. 6). Dilution of individual realizations of the effluent distribution occurs rapidly at the pattern edges mostly due to submesoscale (~km) shredding of the mesoscale (~tens of km) patterns with a straining time scale of $1/\alpha \approx 1$ day (Section 3). Time animations[10] exhibit tidal wobbling in the patterns, but not much associated pattern shredding.

Horizontal maps of the time mean and RMS variability of C (Fig. 8) confirm the strong bathymetric confinement to the shelf and slope. In both bays a mean tongue of C extends past the western bounding headland (Palos Verdes in SPB and Point Dume in SMB), consistent with a westward mean flow during Fall 2006. However, tracers also extend alongshore to the east against this mean flow. The modeled lateral dispersal pattern is qualitatively consistent with a wastewater plume-tracking conducted in May 2000 (Boehm et al., 2002). These facts strongly suggest that the dominant dispersal occurs alongshore in both directions, approximately along isobaths, apparently driven by the prevailing alongshore velocity fluctuations (Fig. 5) associated with reversals of tidal and eddying currents, not by simply following the mean flow. In particular, the importance of mesoscale and submesoscale eddies in dispersion is also evident in Table 1 and in the flow visualization in Figs. 2 and 7. The simplest explanation for the contour-following barotropic flow is that it conserves its potential vorticity, hence is a quasi-stationary, favored dynamical state. Overall the RMS variability is at least as large as the mean except very near the source, and it becomes relatively even larger toward both the coastline and the open sea. At the coast C is not as large as over the middle of the shelf, which indicates an inhibition of cross-

[10] Movies of the full simulations can be seen in the Supplemental Materials at http://www2.kobe-u.ac.jp/~uchiyama/sewage/.

shore transport into very shallow water even in the presence of eddies and tides with cross-shelf flow (Noble et al., 2009b). C also decreases toward deeper water by some combination of a weak cross-shore advection and a high dilution rate further offshore where the eddy currents are stronger.

The tracer concentrations are higher for HTP than OCSD. Partly this is a consequence of the three times larger source strength $\mathcal{Q}_p$ (Section 2.2), but this does not fully account for the even larger difference in C. Furthermore, the HTP patterns more completely fill SMB than OCSD does in SPB. We conclude that SMB is a more sheltered embayment with less effective dispersal and dilution; this is consistent with previous findings that SMB has a much longer tracer residence time (Oram, 2004) than does SPB (Idica, 2010). Also notice the relatively low C values in the northwest corner of SPB that have no counterpart in SMB. Because this corner is not a region of high eddy activity (Fig. 3), hence not a high dilution rate, it must be due to a weak shoreward penetration from the main C tongue over the bathymetric slope contours in the western part of SPB.

Cross-sectional maps of mean and RMS c distributions (Fig. 9) show peaks at the source region and depth z_c and mostly lateral spreading in the injection depth range of $\mathcal{H}(z)$. The spatial maximum of temporal mean $[c](x,z)$ is 0.0021 for OCSD (ten times smaller than the peak value of $c(z,t)$ in Fig. 6, top panel) and 0.0057 for HTP (four times smaller than its peak value). The OCSD-HTP difference in peak mean $[c]$ is consistent with the difference in source strength $\mathcal{Q}_p$, which implies that the dispersal differences between the bays are not very large on average in the nearfield region above the offshore outfalls. On the other hand, the smaller ratio of peak to mean for SMB indicates that its events with the highest rate is smaller than those in SPB.

Offshore the tracer extends seaward well beyond the shelf without much downward transport. Towards the shore there is a weak tendency for the c distribution to climb the shoaling bottom; an analogous descent occurs down the upper slope. Above the source location, c is elevated all the way to the surface, more so in RMS than in mean. This is consistent with episodic entrainment of the nearfield plume by deeper boundary layer mixing. The monitored CDOM data near the transects shown by black lines in Fig. 8 demonstrates that the peak of the mean and RMS of CDOM is centered at $z \approx -38 \pm 5$ m in SMB (City of Los Angeles, 2007; Figs. 3-8 and 3-9) and at $z \approx -46 \pm 5$ m in SPB (Fig. 10; courtesy of B. Jones of USC, *personal communication*). The latter is closely related to the modeled tracer distribution (Fig. 9) with the upslope transport to the shore. The RSB initial dilution model (Roberts et al., 1989) for the OCSD outfall diffusers also confirms that the middle of the plume corresponding to the depth of the minimum dilution is at $z = -36.7 \pm 2.90$ m in 1999 and $z = -38.9 \pm 3.31$ m in 2001 (USGS, 2004; Tables 4-2). These all support a first order accuracy of the simplified near field buoyant stage model employed in the present study.

Local time series and PDFs of C (Figs. 11 and 12) are noticeably different at different sites within the bays, not only in the overall C level (Fig. 8) but also in the character of the temporally intermittent high concentration events associated with eddy transport; these are identified by spikes in $C(t)$ and long tails in $P[C]$. Away from the outfall, the RMS$[C]$ values are at least as large as the mean, and their ratio increases with distance outside the mean-C tongue.

For OCSD along the mean-C tongue (point A with Ku=3.5), there is much less intermittency than in the opposite alongshore direction (point C with Ku=14.3). The low-C northwest corner (point B with Ku=4.2) does not have prominent spikes, suggestive of a diffusive leakage process more than direct tracer filament penetration, although its $P[C]$ also has a long tail to larger C. Offshore (point D with Ku=37.3) the spikes are almost the whole signal. Both points C and D show a much larger ratio between the maximum and mean C values than either along the mean-C tongue or near the source (Fig. 7). For HTP there are similar

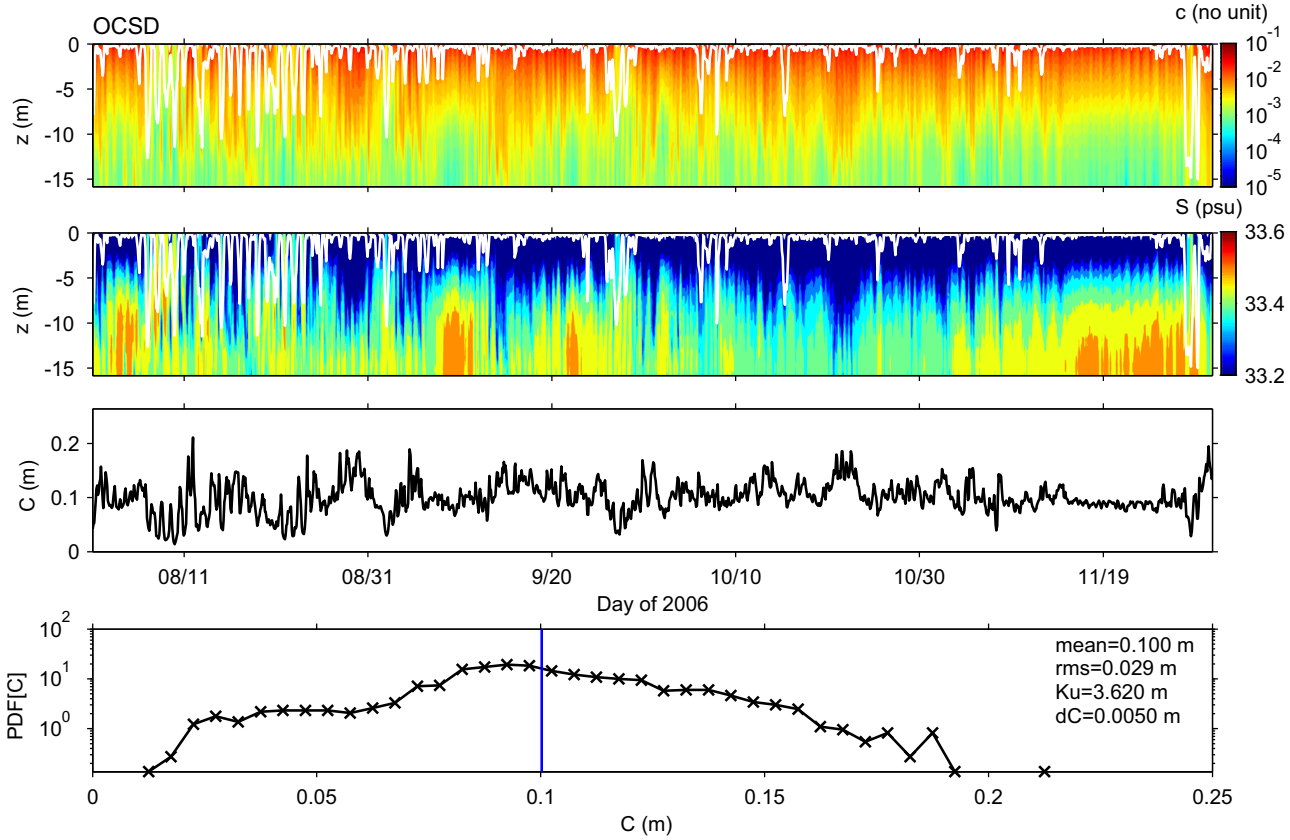

Fig. 14. Source region tracer and salinity for the OCSD nearshore outfall. The format is the same as Fig. 6.

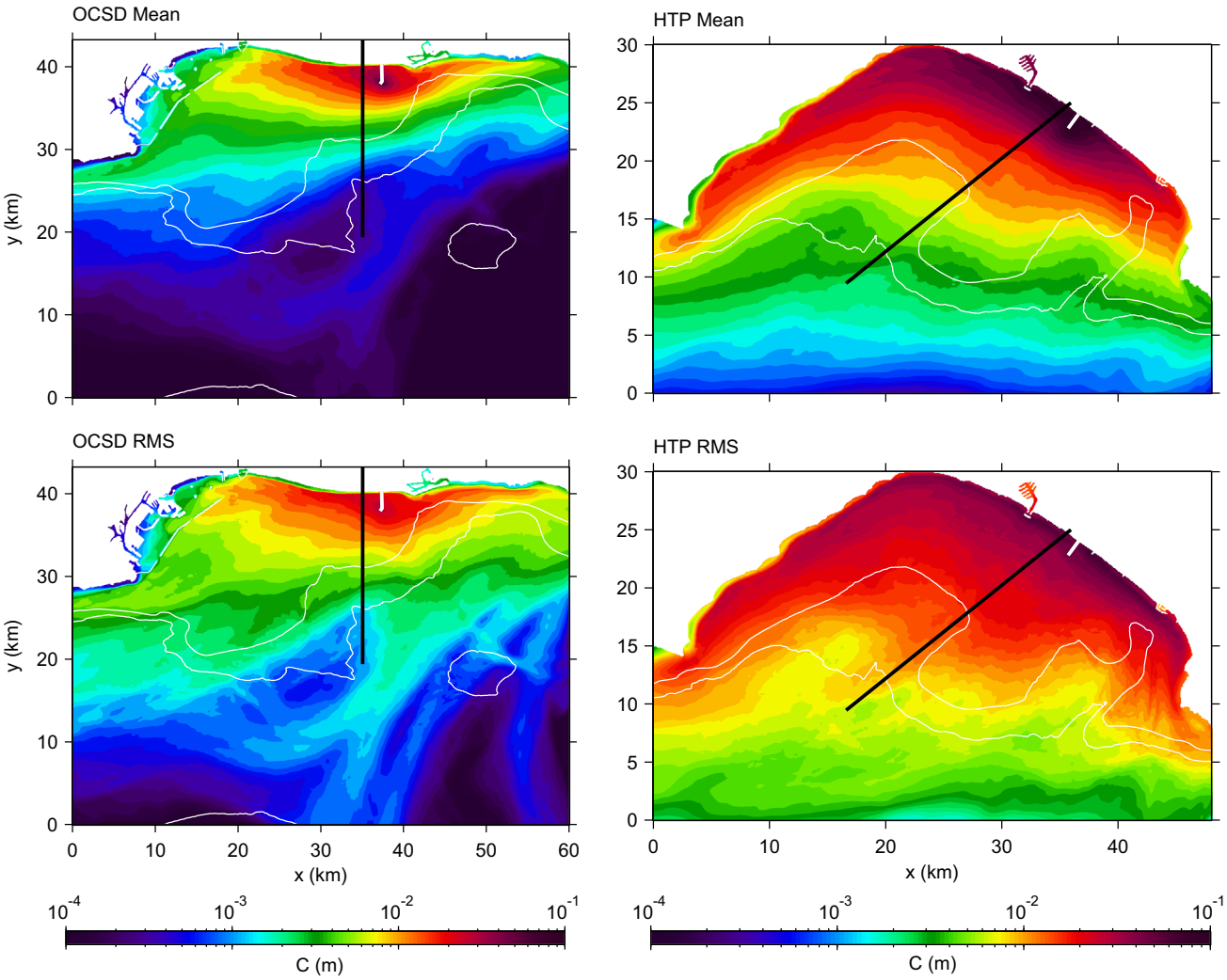

Fig. 15. Mean and RMS of $C(x,y,t)$ for OCSD (left column) and HTP (right) for the nearshore outfalls; *cf.*, Fig. 8 for the offshore outfall. The black lines indicate the vertical sections in Fig. 16.

behaviors. The point B is well within the main mean-C pool and has moderate intermittency (Ku=4.2), but the intermittency increases with distance from the source, both along the mean-C tongue (point A with Ku=7.7), near the coast in the opposite direction (point C with Ku=8.0), and offshore (point D with Ku=15.1).

For the standard outfall locations, the surface layer has smaller C values than the subsurface layer, both in the mean (not shown) and RMS fields (Fig. 13). The spatial patterns are broadly similar between these two layers, although the spatial extent of the patterns is less in the surface layer, indicative of its greater dilution rate in association with its stronger currents (Section 3). Fig. 6 shows that the tracer enters the surface layer during particular events with deeper boundary layer mixing (notice late November). These events will be more frequent in the winter season with surface cooling, weaker stratification, and stormy winds. Hence, the surface pollution levels will probably be higher throughout the winter, but our present simulations do not extend long enough to show this.

5. Effluent distribution: nearshore outfalls

With nearshore outfall pipes, there are two major differences in the effluent dispersal behavior: the nearfield buoyant plume penetrates to the surface (Section 2.2), and the tracer is more confined to the inner shelf adjacent to the shore.

The source region tracer concentration $c(z,t)$ for OCSD is strongly trapped at the surface with somewhat larger values than for the offshore outfalls, and the boundary layer depth is made very shallow because of the buoyant freshwater anomaly in $S(z,t)$ (Fig. 14). The peak value of nearfield $c(z,t)$ is 0.059, about 3 times larger than the peak value for the offshore OCSD outfall (Fig. 6). (The analogous nearshore outfall value for HTP is 0.129, about 6 times larger than its offshore outfall value.) The mean vertically integrated concentration C is only slightly larger than for the offshore outfall (Fig. 6), indicating that nearfield vertical dispersal is less efficient with nearshore outfalls, consistent with the smaller vertical extent of the source function $\mathcal{H}$ (Section 2.2). The variability and intermittency in $C(t)$ and $P[C]$ are somewhat less near the outfall here than for the offshore outfall, but their statistical characteristics (not shown) are similar at the same sites as in Figs. 11 and 12.

The horizontal distributions of the mean and RMS of C (Fig. 15) can reach to the coast[11] in the shoreline sector near the outfall

[11] We reiterate a caution about the limitation of the $dx=75$ m grid resolution in very shallow water ($h<10$ m) and the absence of wave-driven littoral currents in the present model configuration.

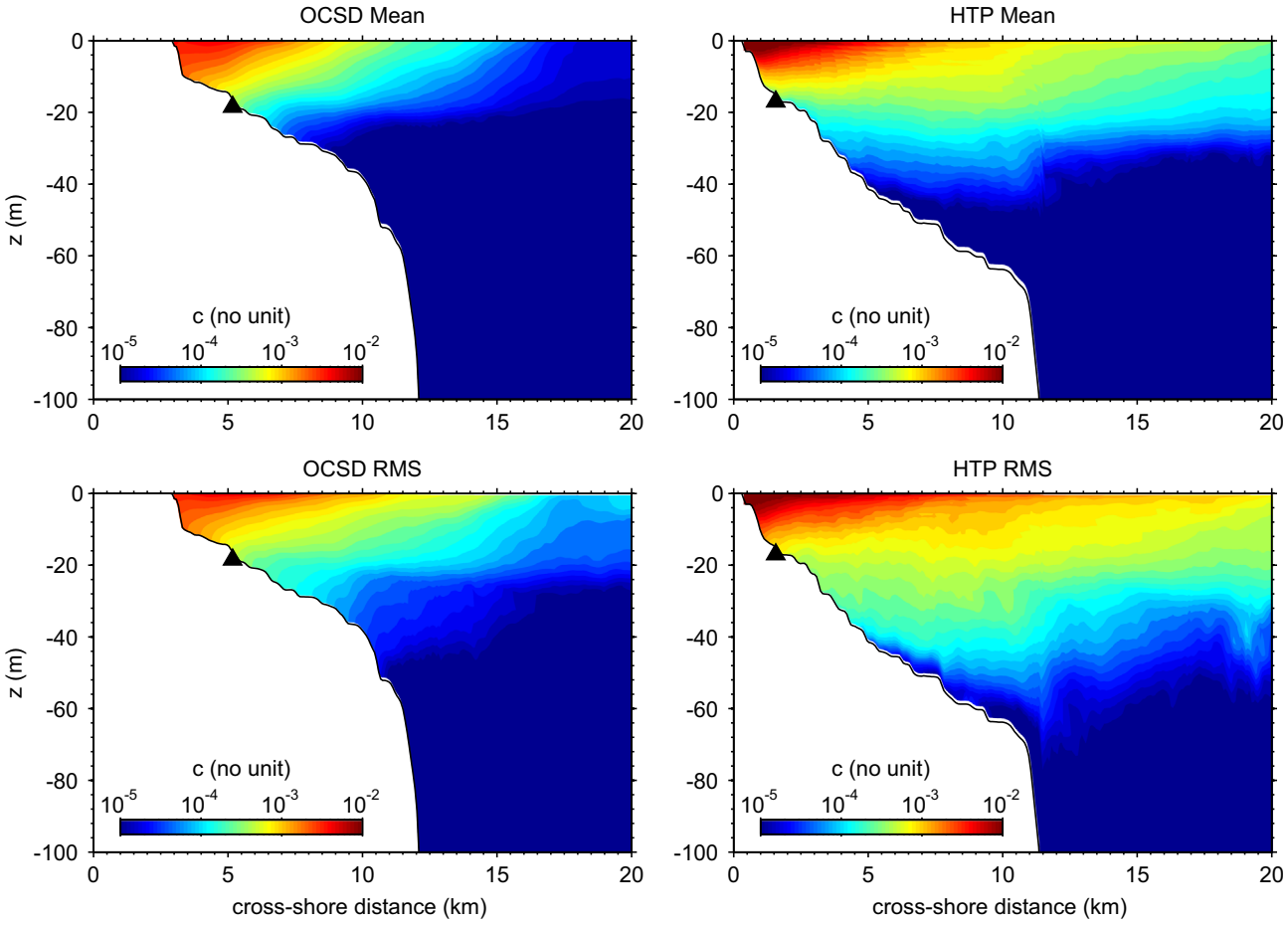

Fig. 16. Mean and RMS of $c(x,z,t)$ for OCSD (left column) and HTP (right) for the nearshore outfalls along the black lines in Fig. 15; *cf.*, Fig. 9 for the offshore outfall. Black triangles indicate the approximate locations of the outfall diffusers.

pipe. They do not extend offshore much beyond the inner shelf where $h \leq 100$ m, but they do extend alongshore over tens of km, comparable to the extent for the offshore outfall (Fig. 8). The RMS variability exceeds the mean C except near the source, and the temporal intermittency (not shown) increases with distance from the source. Both of these characteristics are true as well for the offshore outfalls but to a lesser degree with the nearshore outfalls.

Vertical sections of $c(x,z,t)$ in Fig. 16 clearly show the surface and shoreline confinement, strikingly different from the offshore outfalls (Fig. 9). The spatial maximum of temporal mean $[c](x,z)$ is 0.0048 for OCSD (twice the offshore outfall mean value in Fig. 9) and 0.051 for HTP (about nine times larger than its offshore outfall mean value). The latter ratio indicates that nearshore dispersal is especially inefficient in SMB. In summary, the nearshore outfalls undergo less dispersion and reduced dilution, consistent with weaker flows close to the coast (Section 3).

6. Summary and discussion

Our simulations of effluent dispersal in two Southern California bays are improved in their inclusion of circulation processes. They cover a broader spatial area than has been common in the water-quality monitoring surveys. They provide insight into which currents are most effective in tracer dispersion and dilution, and they demonstrate the potential for full spatial and temporal characterization of pollutants in the environment. The predicted tracer distributions are at least qualitatively consistent with previous measurements (Section 1), and a more quantitative comparison will be made in a companion paper comparing with hydrographic profile and glider measurements. We envision that similar simulations could be adduced for other sites and different emission protocols as a powerful tool for planning and assessment.

After the initial dilution and vertical profiles caused by the nearfield buoyant plumes, subsequent tracer transport is mostly lateral and is dominated by eddy flows, rather than tides or mean currents. The local concentration $c(t)$ in the source region is highly variable due to transport fluctuations, even with little variation in the outfall flux $\mathcal{Q}_p$. The vertical structure of $c(z)$ stays relatively simple and close to the profiles established near the source. For the normal outfall locations, surface-layer concentrations are relatively small, but episodic ventilation events occur, especially when the boundary layer deepens. The lateral transport is highly anisotropic, with alongshore excursions much greater than cross-shore; this is consistent with a statistical analysis of particle-pair dispersion in coastal zone in the Southern California Bight using some of the same simulations (Romero et al., 2013). The peak values of the temporal mean and RMS of $C(x,y) = \int c\, dz$ occur over the middle of the continental shelf and upper part of the continental slope. Shoreward transport is inhibited in shallow water, and offshore concentrations are low because of increased dilution in larger, stronger eddies there. The poleward mean flow gives an up-coast bias to the tracer distribution, but large concentrations are found down-coast as well, spilling over into adjacent regions outside the bays in both directions. Local $C(t)$ values are highly intermittent, with PDFs $P[C]$ showing long tails for large C, and the intermittency increases with distance from the source. Lateral patterns in $C(x,y)$ show stirring by mesoscale

meandering tongues and dilution by submesoscale shredding of the tongues. Tidal currents cause primarily oscillatory displacements and do not effect significant far-field dilution. Peak C values decrease only slowly away from the source region in individual realizations of tracer patterns (Fig. 7), although on longer time scales and distances mesoscale flow reversals do erase previously emitted effluent patterns. That is, dilution is relatively inefficient over several days and the tens of km size of the bays (20–40 km; Figs. 7 and 8). At the pattern edges dilution occurs by submesoscale straining on a time scale of about a day. Dispersal and dilution are relatively more efficient in SPB than in SMB because the former is exposed to stronger mean and eddy flows. From both bays the effluent pattern is advected past Palos Verdes peninsula to add to the contamination in the adjacent bay.

With the nearshore diversion outfalls, the shoreline is much more exposed to the effluent tracers than with the standard offshore outfalls. This occurs by a combination of surface penetration of the nearfield buoyant plumes and weaker eddy currents and weaker dilution over the inner shelf, especially in the cross-shore direction.

Acknowledgments

We thank our colleagues Florian Lemarie, Jeroen Molemaker, and Alexander Shchepetkin for their help in preparing the meteorological fields and developing the modeling capabilities. We also thank Burt Jones (USC, KAUST) and George Robertson (OCSD) for guidance on effluent plumes. We appreciate support from the Office of Naval Research (N00014-12-1-0939), the Orange County Sanitation District, the National Oceanic and Atmospheric Administration (A11NOS0120029) through the Southern California Coastal Ocean Observing System, and the Grant-in-Aid for Scientific Research (24560622).

References

Anderson, J.W., Reish, D.J., Spies, R.B., Brady, M.E., Segelhorst, E.W., 1993. Human impacts. In: Dailey, M.D., Reish, D.J., Anderson, J.W. (Eds.), Ecology of the Southern California Bight. University of California Press, Berkeley, pp. 682–766

Bassin, C.J., Washburn, L., Brzezinski, M., McPhee-Shaw, E., 2005. Sub-mesoscale coastal eddies observed by high frequency radar: a new mechanism for delivering nutrients to kelp forests in the Southern California Bight. Geophys. Res. Lett. 32, L12604.

Becker, J.J., Sandwell, D.T., Smith, W.H.F., Braud, J., Binder, B., Depner, J., Fabre, D., Factor, J., Ingalls, S., Kim, S.-H., Ladner, R., Marks, K., Nelson, S., Pharaoh, A., Trimmer, R., Von Rosenberg, J., Wallace, G., Weatherall, P., 2009. Global bathymetry and elevation data at 30 arc seconds resolution: SRTM30_PLUS. Mar. Geod. 32, 355–371.

Blaas, M., Dong, C., Marchesiello, P., McWilliams, J.C., Stolzenbach, K.D., 2007. Sediment transport modeling on Southern Californian shelves: a ROMS case study. Cont. Shelf Res. 27, 832–853.

Boehm, A.B., Sanders, B.F., Winant, C.D., 2002. Cross-shelf transport at Huntington Beach. Implications for the fate of sewage discharged through an offshore ocean outfall. Environ. Sci. Technol. 36, 1899–1906.

Buijsmann, M.C., Uchiyama, Y., McWilliams, J.C., Hill-Lindsay, C.R., 2012. Modeling semidiurnal internal tide variability in the Southern California Bight. J. Phys. Oceanogr. 42, 62–77.

California Regional Water Quality Control Board (CRWQCB), 2010. A Waste Discharge Requirements and National Pollutant Discharge Elimination System Permit for the City of Los Angeles. Hyperion Treatment Plant Discharge to the Pacific Ocean, Order No. R4-2010-0200, NPDES No. CA0109991.

California Regional Water Quality Control Board (CRWQCB), 2012. A Waste Discharge Requirements and National Pollutant Discharge Elimination System Permit for Orange County Sanitation District Reclamation Plant No. 1 and Treatment Plant No. 2, Order No. R8-2012-0035, NPDES No. CA0110604.

Capet, X.J., Marchesiello, P., McWilliams, J.C., 2004. Upwelling response to coastal wind profiles. Geophys. Res. Lett. 31, L13311/1–L13311/4.

Capet, X., Colas, F., McWilliams, J.C., Penven, P., Marchesiello, P., 2008a. Eddies in eastern-boundary subtropical upwelling systems. In: Hecht, M., Hasumi, H. (Eds.), Eddy-Resolving Ocean Modeling. AGU Monograph, pp. 131–147

Capet, X., McWilliams, J.C., Molemaker, M.J., Shchepetkin, A.F., 2008b. Mesoscale to submesoscale transition in the California Current System. I. Flow structure, eddy flux, and observational tests. J. Phys. Oceanogr. 38, 29–43.

Carr, S.D., Capet, X., McWilliams, J.C., Pennington, J.T., Chavez, F.P., 2008. The influence of diel vertical migration on zooplankton transport and recruitment in an upwelling region: estimates from a coupled behavioral–physical model. Fish. Oceanogr. 17 (1), 1–15.

Carton, J., Giese, B., 2008. A reanalysis of ocean climate using Simple Ocean Data Assimilation (SODA). Mon. Weather Rev. 136, 2999–3017.

City of Los Angeles, 2007. Marine Monitoring in Santa Monica Bay Biennial Assessment Report, January 2005 through December 2006. City of Los Angeles, Department of Public Works, Bureau of Sanitation, Environmental Monitoring Division.

Colas, F., Capet, X., McWilliams, J.C., Li, Z., 2013. Mesoscale eddy buoyancy flux and eddy-induced circulation in eastern-boundary upwelling systems. J. Phys. Oceanogr. 43, 1073–1095, http://dx.doi.org/10.1175/JPO-D-11-0241.1.

Dai, A., Trenberth, K.E., 2002. Estimates of freshwater discharge from continents: latitudinal and seasonal variations. J. Hydrometeorol. 3, 660–687.

Di Giacomo, P.M., Holt, B., 2001. Satellite observations of small coastal ocean eddies in the Southern California Bight. J. Geophys. Res. 106 (C10), 22521–22543.

Di Giacomo, P.M., Washburn, L., Holt, B., Jones, B.H., 2004. Coastal pollution hazards in Southern California observed by SAR imagery: stormwater plumes, wastewater plumes, and natural hydrocarbon seeps. Mar. Pollut. Bull. 49, 1013–1024.

Dong, C., McWilliams, J.C., 2007. A numerical study of island wakes in the Southern California Bight. Cont. Shelf Res. 27, 1233–1248.

Dong, C., Idica, E.Y., McWilliams, J.C., 2009. Circulation and multiple-scale variability in the Southern California Bight. Prog. Oceanogr. 82, 168–190.

Dong, C., McWilliams, J.C., Hall, A., Hughes, M., 2011. Numerical simulation of a Synoptic Event in the Southern California Bight. J. Geophys. Res. 116, C05018.

Durski, S.M., Glenn, S.M., Haidvogel, D.B., 2004. Vertical mixing schemes in the coastal ocean: comparison of the level 2.5 Mellor–Yamada scheme with an enhanced version of the K profile parameterization. J. Geophys. Res. 109, C01015.

Egbert, G., Bennett, A., Foreman, M., 1994. TOPEX/Poseidon tides estimated using a global inverse model. J. Geophys. Res. 99, 24821–24852.

Fischer, H.B., List, E.J., Koh, R.C.Y., Imberger, J., Brooks, N.H., 1979. Mixing in Inland and Coastal Waters. Academic Press, New York

Gruber, N., Frenzel, H., Doney, S.C., Marchesiello, P., McWilliams, J.C., Moisan, J.R., Oram, J.J., Plattner, G.-K., Stolzenbach, K.D., 2006. Eddy-resolving simulations of plankton ecosystem dynamics in the California current system. Part I. Model description, evaluation, and ecosystem structure. Deep Sea Res. I 53, 1483–1516.

Gruber, N., Lachkar, Z., Frenzel, H., Marchesiello, P., Münnich, M., McWilliams, J.C., Nagai, T., 2012. Eddy-induced reduction of biological production in eastern boundary upwelling systems. Nat. Geophys. 4, 787–792.

Hamilton, P., Noble, M.A., Largier, J., Rosenfeld, L.K., Robertston, G., 2006. Cross-shelf subtidal variability in San Pedro Bay during summer, 2001. Cont. Shelf Res. 26, 681–702.

Hickey, B., 1992. Circulation over the Santa Monica-San Pedro basin and shelf. Prog. Oceanogr. 30, 37–115.

Idica, E.Y., 2010. Contaminant Transport in the Southern California Bight (Dissertation). University of California, Los Angeles.

Jones, B.H., 2004. Spatial and temporal pattern of plume tracers. In: Nobel, M., Xu, J. (Eds.), Huntington Beach Shoreline Contamination Investigation, Phase III, Final Report. USGS Open-File Report 04-1019 (Chapter 10).

Jones, B.H., Barnett, A., Robertson, G.L., 2001. Towed mapping of the effluent plume from a coastal ocean outfall. In: MTS/IEEE Oceans 2001. An Ocean Odyssey. Conference Proceedings, vol. 3, pp. 1985–1989.

Kim, S.Y., Terrill, E.J., Cornuelle, B.D., Jones, B., Washburn, L., Moline, M.A., Paduan, J.D., Garfield, N., Largier, J.L., Crawford, G., Kosro, P.M., 2010. Mapping the U.S. West Coast surface circulation: a multi-year analysis of high-frequency radar observations. J. Geophys. Res. 116, C03011.

Kurian, J., Colas, F., Capet, X., McWilliams, J.C., Chelton, D.B., 2011. Eddy properties in the California current system. J. Geophys. Res. 116, C08027.

Large, W.G., McWilliams, J.C., Doney, S., 1994. Oceanic vertical mixing: a review and a model with a nonlocal boundary layer parameterization. Rev. Geophys. 32, 363–403.

Marchesiello, P., McWilliams, J.C., Shchepetkin, A., 2003. Equilibrium structure and dynamics of the California Current System. J. Phys. Oceanogr. 33, 753–783.

Mason, E., Molemaker, J., Shchepetkin, A.F., Colas, F., McWilliams, J.C., Sangrà, P., 2010. Procedures for offline grid nesting in regional ocean models. Ocean Model. 35, 1–15.

Michalakes, J., Dudhia, J., Gill, D., Klemp, J., Skamarock, W., 1998. Design of a next-generation regional weather research and forecast model. In: Proceedings of the Eighth Workshop on the Use of Parallel Processors in Meteorology. European Center for Medium Range Weather Forecasting, Reading, United Kingdom, pp. 117–124.

Mitarai, S., Siegel, D.A., Watson, J.R., Dong, C., McWilliams, J.C., 2009. Quantifying connectivity in the coastal ocean with application to the Southern California Bight. J. Geophys. Res. 114, C10026.

Molemaker, M.J., McWilliams, J.C., Dewar, W.K., 2014. Submesoscale generation of mesoscale anticyclones in the California Undercurrent. J. Phys. Oceanogr., submitted for publication.

Noble, M., Rosenberger, K.J., Hamilton, P., Xu, J.P., 2009a. Coastal ocean transport patterns in the central Southern California Bight. In: Lee, H.J., Normak, W.R. (Eds.), Earth Science in the Urban Ocean: The Southern California Continental Borderland. Geological Society of America Special Paper, pp. 193–226.

Noble, M., Jones, B.H., Hamilton, P., Xu, J., Robertson, G., Rosenfeld, L., Largier, J., 2009b. Cross-shelf transport into nearshore waters due to shoaling internal tides in San Pedro Bay, CA. Cont. Shelf Res. 29, 1768–1785.

Oram, J.J., 2004. A Multi-Disciplinary Investigation of the Dynamics of Surface Waters in the Southern California Bight (Dissertation). University of California, Los Angeles.

Orange County Sanitation District (OCSD), 2012. Ocean Monitoring Annual Report 2010–2011.

Penven, P., Debreu, L., Marchesiello, P., McWilliams, J.C., 2006. Evaluation and application of the ROMS 1-way embedding procedure to the California Current Upwelling System. Ocean Model. 12, 157–187.

Roberts, P.J.W., Snyder, W.H., Baumgartner, D.J., 1989. Ocean outfalls: I. Submerged wastefield formation and II. Spatial evolution of submerged wastefield and III. Effect of diffuser design on submerged wastefield. J. Hydrol. Eng. 115, 1–25 26–48 and 49–70.

Romero, L.E., Uchiyama, Y., Ohlmann, C., McWilliams, J.C., Siegel, D.A., 2013. Particle-pair dispersion in the Southern California coastal zone. J. Phys. Oceanogr. 43, 1862–1879.

Shchepetkin, A.F., McWilliams, J.C., 2005. The regional ocean modeling system: a split-explicit, free-surface, topography-following-coordinate oceanic model. Ocean Model. 9, 347–404.

Shchepetkin, A.F., McWilliams, J.C., 2008. Computational kernel algorithms for fine-scale, multiprocess, longtime oceanic simulations. In: Temam, R., Tribbia, J. (Eds.), Handbook of Numerical Analysis. Elsevier, Amsterdam, pp. 119–181

Sklar, A., 2008. Brown Acres: an Intimate History of the Los Angeles Sewers. Angel City Press, Santa Monica, CA p. 232

Southern California Coastal Water Research Project (SCCWRP), 1973. The Ecology of the Southern California Bight: Implications for Water Quality Management. Technical Report 010. Southern California Coastal Water Research Project. El Segundo, CA, p. 566.

Todd, R.E., Rudnick, D.L., Davis, R.E., 2009. Monitoring the greater San Pedro Bay region using autonomous underwater gliders during fall of 2006. J. Geophys. Res. 114, C06001.

USGS, 2004: Huntington Beach Shoreline Contamination Investigation, Phase III, Final Report. In: Noble, M., Xu, J. (Eds.), USGS Open-File Report, 04-1019, p. 342.

Wang, X., Chao, Y., Dong, C., Farrara, J., Li, Z., McWilliams, J.C., Paduan, J.D., Rosenfeld, L.K., 2009. Modeling tides in Monterey Bay, California. Deep-Sea Res. II 56, 219–231.

Weil, J.C., Sullivan, P.P., Patton, E., Moeng, C., 2012. Statistical variability of dispersion in the convective boundary layer: ensembles of simulations and observations. Bound.-Layer Meteorol. 145, 185–210.